

**MGO DOPED PPLN OPTICAL WAVELENGTH
CONVERTER WITH AN INTEGRATED STRUCTURE**

**MGO DOPED PPLN OPTICAL WAVELENGTH
CONVERTER WITH AN INTEGRATED STRUCTURE**

By

JUAN DENG, B.Sc

A Thesis

Submitted to the School of Graduate Studies

In Partial Fulfilment of the Requirements

For the Degree

Master of Applied Science

McMaster University

© Copyright by Juan Deng, April 2008

MASTER OF APPLIED SCIENCE (2008)
(Engineering Physics)

McMaster University
Hamilton, Ontario

TITLE: MgO doped PPLN optical wavelength converter with an integrated structure

AUTHOR: Juan Deng
B.Sc. (University of Science and Technology of China)

SUPERVISOR: Professor C.Q.Xu

NUMBER OF PAGES: x, 72

Abstract

This thesis describes the development of optical wavelength converters with an integrated coupling structure, fabricated on periodically poled MgO doped lithium niobate (MgO:LN) for optical fiber communication and other all-optical signal processing applications. Wavelength converter is an integral part of any broadband communication system. The ability to transfer information between carrier wavelengths allows for efficient use of the available bandwidth in a transmission medium. Wavelength converters based on PPLN waveguides are among the most efficient nonlinear optical devices available today, due to high-speed operation, low noise, parallel operation on multiple wavelength channels and preservation of information carried in the optical domain. However, low conversion efficiency is an issue for wavelength converter based on PPLN waveguide. Compared to pure LN, MgO doped LN decrease restriction in optical damage and increase conversion efficiency. Integrated coupling structure demonstrates a solution to mode-coupling of the input wave to the fundamental mode of DFG device and increase the conversion efficiency. Therefore, a periodically poled MgO doped lithium niobate (MgO:LN) waveguides with integrated coupling structure is fabricated. The components of integrated coupling structure are compatible with lithium niobate waveguides, including directional couplers, small radius bends, adiabatic taper, and mode filter. The integrated coupling structure combines the pump and signal waves into the DFG conversion section, and makes the single mode conversion of the pump from input waveguide to conversion section. Theoretical models and simulations are provided in this thesis, and performances of the device with this structure are also presented.

Acknowledgement

This work would not have been possible without the support and encouragement of my colleagues, friends and family. I would like to thank all the people who helped me in the past two years.

Foremost, I would like to thank my supervisor Prof. Chang-Qiang Xu, who shared with me a lot of his research insight and life wisdom. His tremendous enthusiasm and dedication to research has made him the role model of a successful researcher in the field. His patience in clarifying things simply and sound advices showing senses of research direction have been abundantly helpful during my studies. I am also thankful to him for boosting optimism and my self-confidence during hard times. Without his support and encouragement, I would not have gotten this far.

I would like to thank the other members of my thesis defence committee: Prof. Xun Li and Prof. Qiyin Fang for accepting the responsibility on a short notice, and all the comment throughout the experience. Special thanks to Prof. Li for helpful discussions on the device design.

I would like to thank the many people involved in the project, without whom this work could not have been completed. Thanks to Dr. Wanguo Liang for dedication in device fabrication and all the collaboration that made the work possible. Working with Dr. Jian Yang was a pleasure, and I appreciate him for developing the external cavity laser diode with FBG, as well as for many helpful discussions on the device measurement and result analysis. Thanks to Prof. Paul Jessop for lending me the simulation software BPM-CAD.

I would like to thank my fellow graduate students, Yi Gan, Jorge Fonseca Campos, Bo Chen, Qingyang Xu, Ling Han, and my lab mates Dr. Yong Wang, Fangfang Zhang. Their friendship and assistance made my days in this group a pleasant memory.

I would like to thank all of my friends throughout my education. They have always been important to me.

I cannot finish without saying how grateful I am with my husband for all his love and support. There were many times that I wanted to abandon my research, and he helped me to persevere and finish every step.

Table of Contents

1. Introduction	1
1.1 WDM network	1
1.2 Wavelength conversion mechanisms.....	2
1.3 Motivation.....	7
1.4 Overview.....	9
2. Theory of guided-wave quasi-phase-matched wavelength conversion	11
2.1 Difference Frequency Generation and Second Harmonic Generation (DFG & SHG)	11
2.2 Maxwell's Equations.....	13
2.3 Coupled-mode equation.....	14
2.4 Quasi-Phase Matching (QPM)	17
2.5 Waveguide.....	20
3. Device fabrication and waveguide modeling	24
3.1 lithium niobate (LN)	24
3.2 Fabrication of QPM waveguide devices.....	25
3.3 Modeling of refractive index profile for APE LN waveguide	27
3.4 Sellmeier equation.....	30
4. Design of integrated coupling structure	33
4.1 Introduction.....	33
4.2 integrated coupling structure.....	34
4.3 Mode-filters and input tapers.....	36
4.4 Directional coupler.....	39
4.5 Small radius bending.....	44
4.6 Modeling of the device structure.....	48
5. Wavelength converter with integrated coupling structure	53
5.1 Basic device information.....	53
5.2 Loss measurement.....	53
5.3 SHG measurement.....	54
5.4 External cavity Laser diode with fiber Bragg grating.....	58
5.5 Fiber Bragg grating.....	61
5.6 DFG measurement.....	63
6. Conclusion	68
6.1 summary of Research Contributions.....	68
6.2 future research.....	69

List of Figures and Tables

Fig.1.1: simple point-to-point WDM transmission system.....	1
Figure 1.2: (a) Network blocking probabilities can be resolved by wavelength-conversion function. (b) Distribution of network control and management into smaller sub-networks utilizes wavelength conversion. Network operators 1, 2, and 3, are responsible for their own sub-networks, and wavelength assignments within the sub-networks are independent of each other.....	2
Fig.1.3: Functional block diagrams of a) optoelectronic, b) optical grating, and c) wave mixing (e.g. difference-frequency-generation, four wave mixing) wavelength converters.....	3
Fig.1.4: schematic diagram of four-wave-mixing in frequency domain.....	7
Fig.1.5: device structure of QPM-LN wavelength converter.....	8
Fig.1.6: schematic diagram of a) direct DFG, b) cascaded SHG: DFG, c) cascaded SFG: DFG. In SFG:DFG scheme, SFG process takes place between two pump or one pump and the signal.....	8
Fig.2.1: a) Geometry of second harmonic generation. b) Energy-level diagram describing second-harmonic generation.....	12
Fig.2.2: Schematic descriptions of difference-frequency generation between a pump at ω_p and a signal at ω_s	12
Fig.2.3: Effects of phase mismatch on the conversion efficiency.....	17
Fig.2.4: Diagram of quasi-phase matching plotting the second harmonic signal for the conditions of: A. Perfect phase matching, C. No phase matching, B1. First-order QPM, and B3.Third-order QPM.....	18
Fig.2.5: Square-shaped modulation of the nonlinear coefficient $d(x)$ for quasi-phase matching.....	19
Fig. 2.6: Slab optical waveguide: a) basic structure, b) index profile of step-index type, and c) graded-index type.....	20
Fig. 2.7: Zig-zag propagating path of light along optical waveguides for different modes.....	22

Fig.2.8: wave-vector diagram.....	22
Fig.2.9: Typical structures of optical channel waveguides: a) buried type, b) ridge type. ($n_f > n_s$).....	23
Fig.3.1: Device fabrication process chart.....	25
Fig.3.2: Micrograph of PPLN surface after etching in hydrofluoric acid. Domains of reserved polarity are etched, while original domains are not, such that domain boundaries are revealed as lines.....	26
Fig.3.3: a) PE and b) APE index and mode profiles in the depth dimension. The gray layer represents the exchanged step index profile.....	28
Fig.3.4: Coordinate system of the model and the crystal axes.....	29
Fig.3.5: (a) index distribution of $8 \mu\text{m}$ -wide waveguide cross section, (b) simulation results of fundamental mode profile.....	30
Fig.4.1: Schematic drawing of mode-launching issues. A single-mode waveguide for the signal wavelength supports multimodes for the pump wavelength.....	33
Fig.4.2: schematic diagram of DFG wavelength conversion device including integrated coupling structure.....	35
Fig.4.3: Micrograph of integrated coupling structure on PPLN waveguide device: a) part of adiabatic taper and bending, b) part of directional coupler. The domain walls are vertical straight lines and light propagates horizontally along waveguides. W is the waveguide width $\sim 8 \mu\text{m}$, Λ is the QPM period $\sim 19.5 \mu\text{m}$ and G is the gap between two adjacent waveguide $\sim 2.5 \mu\text{m}$	35
Fig.4.4: measured mode profile at $\lambda = 780\text{nm}$ for waveguide mask width of $2 \mu\text{m}$	36
Fig.4.5: Measured mode profiles at $\lambda = 1550\text{nm}$ in the wavelength conversion section with waveguide mask width of $8 \mu\text{m}$	37
Fig.4.6: Measured mode profiles at $\lambda = 780\text{nm}$ in the multi-mode section with waveguide mask width of $8 \mu\text{m}$	37
Fig.4.7: schematic plot of two different adiabatic taper in waveguide: a) segmented structure and b) continuous lateral taper.....	38

Fig. 4.8: Taper types of a) linear, b) S-sin, C) exponential.....	38
Fig.4.9: Normal modes in two waveguide in the absence and presence of coupling	40
Fig.4.10: Operating principle of waveguide directional coupler.....	40
Fig.4.11: explanation of integration for calculation of coupling coefficients.	42
Fig.4.12: simulation of power transfer for directional coupler.....	42
Fig.4.13: simulated coupling lengths vs. waveguide separation for waveguide width of $9\ \mu\text{m}$	43
Fig.4.14: Measured coupling ratio of signal with $\lambda=1550\text{nm}$ into conversion section as a function of coupler length (cm) for coupler waveguide width of a) $8\ \mu\text{m}$, b) $8.5\ \mu\text{m}$, c) $9\ \mu\text{m}$ while keeping waveguide separation of $2.5\ \mu\text{m}$	44
Fig.4.15: fiber array made of V-groove.....	45
Fig.4.16: Corner-bent waveguide for path bending.....	45
Fig.4.17: S-Shaped waveguides for path bending.....	46
Fig.4.18: Simulation of electric field distribution in a) circular bending, b) S-Sin bending and c) S-Cos bending waveguides with $l=3.5\ \text{cm}$	47
Fig.4.19: Bending loss vs. bending length for circular, S-cos and S-sin bends....	48
Fig.4.20: BPM layout for integrated structure.....	49
Fig.4.21: Optical field distribution of the signal light propagation.....	50
Fig.4.22: Optical field distribution of the pump light propagation.....	50
Fig.5.1: Schemes of misalignments between fiber and waveguide. a) transverse misalignment, given by the offset d between the centers of the fiber and the waveguide. b) longitudinal misalignment, given by the gap g between the fiber and the waveguide, c) angular misalignment, given by the angle θ of facets of the fiber and waveguide end.	54

Fig.5.2: Measured CW SHG tuning curve (circle marks) and theoretical sinc ² tuning curve (dashed line). Distortion is observed between measurement and calculation.	55
Fig. 5.3: Spectrum of a) fundamental wave and b) second harmonic wave measured at output of the device.....	56
Fig.5.4: SHG power as functions of input pump power. The data fit well with the calculation.	57
Fig.5.5: Temperature tuning curve for PPMgO:LN with QPM period $\Lambda = 19.5\mu m$	58
Fig.5.6: Block diagram of external cavity Laser diode with FBG.....	58
Fig.5.7: Experimental setup of the external cavity Laser diode with FBG.....	59
Fig.5.8: The measured transmission spectrum of the FBG.	60
Fig.5.9: Typical emission spectrum of the Fabry-Perot Laser diode a) with FBG stabilization, b) without FBG stabilization.....	60
Fig.5.10: a) typical fiber Bragg grating structure and b) refractive index profile..	61
Fig.5.11: Phase mask grating fabrication.....	63
Fig.5.12: Schematic diagram for DFG wavelength conversion measurement. FBG: fiber Bragg grating. PC: polarization controller. OSA: optical spectrum analyzer.	64
Fig.5.13: Experimental setup for DFG wavelength conversion measurement....	65
Fig.5.14: Measured optical spectrum of a DFG experiment on a logarithmic scale of a signal at 1524.6nm and its converted output at 1610.4nm.	66
Fig.5.15: Relative conversion efficiency as a function of input signal wavelength. The cross marks are measured result, and the solid line is the theoretical prediction. The device has a 3-dB conversion bandwidth of 94 nm.	67
Table 1: Comparisons of various wavelength conversion techniques.....	4
Table 2: Parameters for Sellemier equation (3.11)	31

Chapter 1

Introduction

In recent years, an explosion of data traffic due to increased use of the internet and commercialized multimedia services is driving force for high capacity and flexibility of optical backbone networks at ever-decreasing cost. Low-loss single mode optical fiber deployed in telecommunications network has been fabricated with bandwidth exceeding several terahertz.[1] However, such enormous bandwidth is under-utilized by a typical telecommunication system of 10 Gbit/s commercially available today. Wavelength division multiplexing (WDM) technology offers an effective solution to utilize the existing embedded fiber bandwidth directly in the wavelength domain, and allows for a multiplication in capacity while keeping costs low. Wavelength conversion device is required to process the transmission signal and make the flexible and efficient network technology possible. Therefore, the development of wavelength converter has been accelerated recently.

In this chapter, a brief description of WDM network is presented. Several wavelength conversion techniques are described and compared. The motivations of this research are explained and followed by an overview of this thesis.

1.1 WDM network

In WDM systems, multiple independent information channels are transmitted simultaneously on a single fiber by using different optical wavelengths for each channel. A schematic diagram of simple point-to-point WDM system is shown in Fig.1.1, where a multiplexer at the transmitter of one node is used to join the signals together, and a demultiplexer is used to split them apart at the receiver of a destination node. The minimum spectral separation between different signal channels is determined by the bit rate of each signal and desired bit-error rate (BER) which is relevant to the crosstalk between each channel. For example, the transmission of 160 signal channel at 10 Gbit/s over 321 km in a single fiber has been demonstrated in a Dense WDM (DWDM) system, which expands a basic 10 Gbit/s fibre system to a theoretical total capacity of over 1.6 Tbit/s [2].

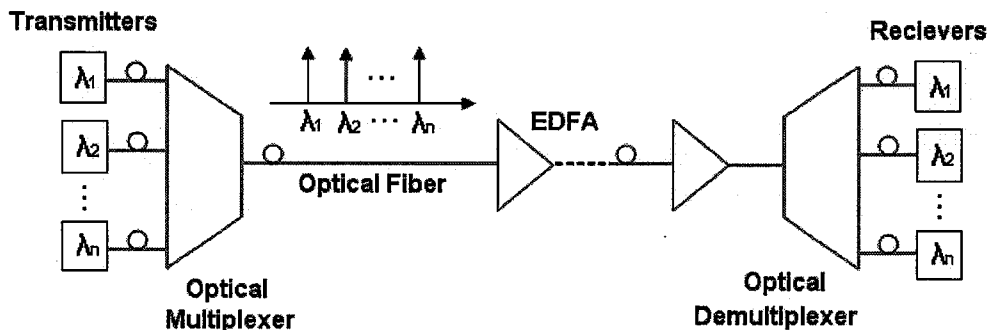


Fig.1.1 simple point-to-point WDM transmission system

In WDM network with multi-users, the number of available wavelengths is not large enough to support a large number of nodes. In such case, blocking probability rises due to possible wavelength contention when two channels at the same wavelength are to be routed into the same output. Functions, such as switching, wavelength adding/dropping, wavelength conversion, etc., are required beyond those required for WDM point-to-point connection. As one of the most important functions in transparent WDM network, wavelength conversions decrease the wavelength contention and blocking probability, and make it possible to reuse wavelengths and establish a flexible and easy manageable wavelength routing networks. Wavelength conversion function is illustrated in Fig.1.2 (a), distribution of the network control and management into small sub-network utilizing wavelength conversion is shown in Fig.1.2 (b).

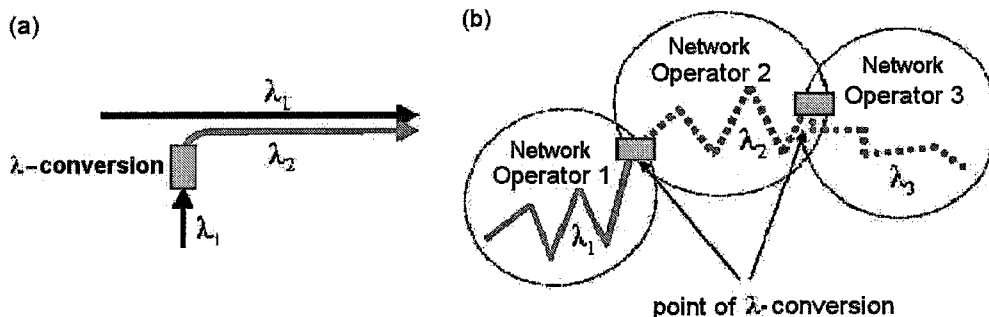


Figure 1.2 (a) Network blocking probabilities can be resolved by wavelength-conversion function. (b) Distribution of network control and management into smaller sub-networks utilizes wavelength conversion. Network operators 1, 2, and 3, are responsible for their own sub-networks, and wavelength assignments within the sub-networks are independent of each other. [3]

There are several issues that need to be considered in proposing wavelength conversion techniques. These issues can be grouped in three categories: signal quality, configuration and performance[4]. Signal quality includes signal-to-noise ratio, chirp, amplitude distortion and extinction ratio. It largely determines the bit-error-rate and cascability of wavelength converters. Configuration is related to the actual mapping function of the wavelength converter in WDM network. It includes dynamic ranges of input signals, polarization dependence, filtering requirements, control and stability etc. Lastly, the performance includes conversion efficiencies, conversion bandwidths, bit rate limit, and transparency to signal format. Some of the issues are related to each other, and a wavelength converter balance out the advantages and disadvantages according to network application.

1.2 Wavelength conversion mechanisms

Several techniques have been proposed and studied to achieve wavelength conversion. Depending on the mapping functions and the form of control signals,

wavelength converters can be categorized into three types: optoelectronic, optical grating and wave mixing converters. The latter two types are all-optical converters when considering signal routing mechanisms. Fig.1.3 shows functional block diagrams for the three types of wavelength converters. Table 1 summarizes the features of different wavelength conversion technologies, which will be discussed in detail in the following part.

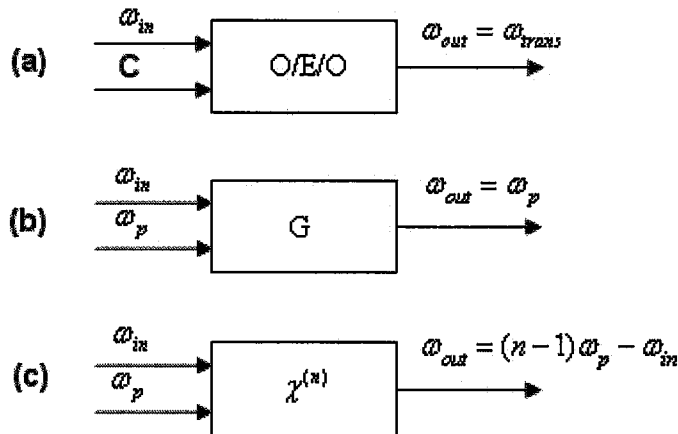


Fig.1.3 Functional block diagrams of a) optoelectronic, b) optical grating, and c) wave mixing (e.g. difference-frequency-generation, four wave mixing) wavelength converters.[4]

Optoelectronic wavelength conversion is conventional and the most straightforward conversion technique where optical signals are converted to electrical signals (O/E) and reconverted to optical signals of different wavelengths (E/O). The optoelectronic wavelength conversion technique is more mature and more readily applicable compared to all optical converters, as it uses conventional O/E devices, such as laser diodes, photodiodes, and integrated circuits. It accommodates wide optical power levels and requires no filtering or polarization control, and the signal regeneration adds flexibility of network control. However, there are shortcomings associate with this technique. The first limitation is the limited transparency of signal format. The information in the form of phase, frequency and analog amplitude is lost during the conversion process. In addition, the speed limitation becomes a bottleneck in the communication system.

Table 1 Comparisons of various wavelength conversion techniques[4, 5]

	OE/EO type	All-optical type				
		Optical gating type			Optical mixing type	
		Cross gain modulation (XGM)	Cross phase modulation (XPM)	Differential phase modulation (DPM)	Four wave mixing (FWM)	Difference frequency generation (DFG)
Typical devices	PD/IC/LD (LD+MD)	SOA LD	SOA + Mach-Zehnder interferometer	SOA + Mach-Zehnder interferometer	Fiber SOA	QPM-LN
Bit rate	~ 40 Gbit/s (IC dependent)	~ 40 Gbit/s (RZ -> NRZ)	~ 40 Gbit/s	~ 160 Gbit/s	~ 1 Tbit/s	~ 1 Tbit/s
Bandwidth	Dependent on light source	Gain bandwidth (~30nm)	Gain bandwidth (~30nm)	Gain bandwidth (~30nm)	~ 40 nm	~ 60 nm
Conversion efficiency	Excellent	Good	Good	Good	Fair	Fair
Polarization insensitivity	Excellent	Good	Good	Good	Fair	Fair
Input level	Receiver dependent (~17 dBm @ 10 Gbit/s)	-10dBm @ 2.5 Gbit/s ~5dBm @ 40 Gbit/s	-10dBm @ 10Gbit/s ~8dBm @ 40 Gbit/s	0~5 dBm @ 40 Gbit/s	~ 20 dBm (SOA+DFB)	-15~5 dBm
Advantages	Ready for deployment	Simple configuration	Reduced chirp, distortion	Higher bit rate	-Chirp reversal -transparent	-Chirp reversal - Transparent -No excess noise -Broad bandwidth
Issues	-Dependent on bit rate and format -Cost increase with bit-rate and number of elements	-High noise Figure, distortion, and chirp - limited transparency	-Narrow input dynamic range -limited transparency	-Narrow input dynamic range -Operation stability	-Low conversion efficiency and bandwidth -Polarization dependent -large spontaneous noise	-Low conversion efficiency - Polarization dependent

While optoelectronic wavelength converter will remain important in the future, all-optical techniques are expected to fully exploit the transmission bandwidth of optical fibers. In all-optical wavelength conversion, optical signals are directly converted to different wavelength signals and no O/E or E/O devices are needed, which greatly enhances conversion speed. It is independent of signal

formats and bit rates, making photonic network transparent with respect to these properties. All-optical converters can be categorized as optical grating converters and optical mixing converters.

Optical grating converter:

Optical gating converter is probably the most widely studied and implemented due to its simplicity and compactness. It includes cross-gain modulation (XGM) in semiconductor optical amplifiers (SOAs), cross-phase modulation (XPM) in SOAs, differential-phase modulation (DPM) in SOAs, and nonlinear optical loop mirror (NOLM) with the nonlinearity achieved by using a length of fiber or SOA.

In XGM scheme, the gain in an SOA saturates as the optical input power increase due to carrier depletion, acting as an optical gate in response of optical input power. At the gain modulation by input signal at λ_1 , a CW wave at λ_2 traveling through the SOA receives no amplification when signal power is high and is conversely amplified when signal power is low. Thus, the information is transferred from wavelength λ_1 to wavelength λ_2 .

XGM is popular due to its simplicity, polarization independency, insensitivity to input wavelength and reasonably high conversion efficiency. However, the conversion speed and bit rate in XGM are limited by carrier lifetime. The output signal exhibits wavelength chirping which is associated with the corresponding refractive index change in SOA. The signal-to-noise ratio (SNR) is degraded due to amplified spontaneous emission (ASE), and extinction ratio is degraded particularly when converting from shorter to longer wavelengths.

To overcome the extinction ratio degradation and reduced chirp associated with XGM in SOAs, XPM in SOAs based on interference switch can be utilized. In the XPM schemes, input signal power modulates the carrier density and refractive index of the SOA. The phase modulation induced by refractive index change is then mapped onto an optical wave travelling through the SOA. This phase modulation can be converted to intensity modulation through a Mach-Zehnder interferometer or Michelson interferometer. Because the interferometer configuration of XPM, the characteristics of the XPM converter depend on input signal intensity, and the dynamic range of input signal intensity is about 2-3 dB, which is comparatively narrow. Accurate control of SOA bias is required due to dependence of phase shift experienced by a signal passing through the SOA on the bias point. The waveform of converted output signals at high bit rate degrades due to the limit of carrier relaxation time in SOA.

A DPM-type wavelength converter can overcome the response speed limitation by the carrier lifetime in the XGM and XPM converter. In DPM scheme, original signal and delayed signal are incident to the SOAs of the two arms of XPM interferometer, so that the lights are phase modulated at each SOA. This method cancels out the effect of slow carrier relaxation time in an SOA and enables higher bit-rate wavelength conversion.

Optical mixing converter:

Optical mixing converter is based on nonlinear optical response of a medium at the presence of more than one wave. The intensity of the generated wave is proportional to intensities of the interacting waves, while the phase and frequency is a linear combination of those interacting waves. Therefore, phase and amplitude information is preserved, making optical mixing converters strict transparent to signal format. Moreover, it enables wavelength conversion with wide wavelength bandwidth, at very high bit rates (Tbit/s-class), and simultaneous multi-wavelength conversion. The nonlinear parametric process is classically free of excess noise unless an active material is used, and the chirp is reversed during the conversion process. However, the polarization control and phase matching are necessary for optical mixing conversion. Optical mixing converters include difference-frequency generation (DFG) scheme and four-wave mixing (FWM) scheme.

DFG is based on second order nonlinear effects in nonlinear materials such as lithium niobate. When the signal wave at ω_s and pump wave at ω_p are incident to a second-order nonlinear material, the converted wave $\omega_p - \omega_s$ is output. DFG has large wavelength conversion range, is capable to simultaneously convert multiple input wavelengths, and free of additional satellite wave appearing in FWM that will interfere with other WDM channels (shown in Fig.1.4). For highly efficient wavelength conversion, phase matching among the signal, pump, and converted waves is required. Therefore, a periodic domain inversion structure is carefully fabricated for quasi-phase matching (QPM) in most of the devices for DFG. In addition, it is important to increase the length of the uniform QPM optical waveguide, improve the optical damage tolerance, and reduce polarization.

FWM are based on third order nonlinear effects and an optical fiber and an SOA are typically used as nonlinear materials. Pump wave at ω_p and signal wave ω_s are incident into a third order nonlinear material and form a grating, the generated wave at $2\omega_p - \omega_s$ is the result of the pump wave scattered by the grating, the satellite wave at $2\omega_s - \omega_p$ is the result of the signal wave scattered by the grating. Fig. 1.4 illustrate schematic diagram of four-wave-mixing in frequency domain. The intensity ratio of the generated waves and the satellite waves equals to that of the pump and the signal.

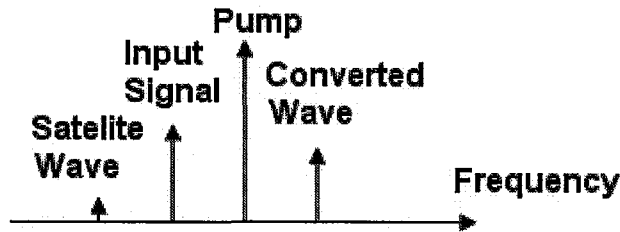


Fig.1.4 schematic diagram of four-wave-mixing in frequency domain [4]

Because the pump wave, signal wave, and converted waves are in the same wavelength band, the phase matching is not as important as it is in DFG. However, as the satellite wave and the pump wave can overlap in wavelength with another WDM channel, filtering has to be carefully executed to avoid crosstalk noise. In addition, input signal wave and the pump wave must have the same polarization. The conversion efficiency is low and decreases as the increase of difference between signal wavelength and pump wavelength. For practical use, it is important to increase conversion efficiency, broaden bandwidth, and reduce polarization sensitivity.

1.3 Motivation

Among the wavelength conversion technologies discussed in 1.2, we have been pursuing the DFG technique based on second order nonlinear effect because it has unique features that are unavailable in other technique. Unlike FWM, the DFG technique do not create additional satellite wave that will interfere with other WDM channel. It has negligible amplified spontaneous emission (ASE) noise, presents no signal-to-noise (S/N) ratio degradation, and offers strict transparency to amplitude, frequency, and phase information. It has extremely high input dynamic range, simultaneously up- or down- convert multiple input WDM channels to different wavelengths. It has potentially high conversion efficiency and wide wavelength bandwidth, can convert high-speed signals of 1THz or greater. In addition, the conversion process generates chirp-reversed signal output, which can be used to perform dispersion compensation fiber links. Therefore, it will be key devices in future photonic networks.

Wavelength conversion devices based on DFG technique have been widely studied and most of them employ quasi-phase-matched lithium niobate (QPM-LN) waveguide. Fig.1.5 shows a basic structure of the wavelength conversion device.

Wavelength converters based on second order nonlinear effect can be implemented by different schemes: direct DFG, cascaded SHG: DFG, and cascaded SFG: DFG, shown in Fig.1.6.

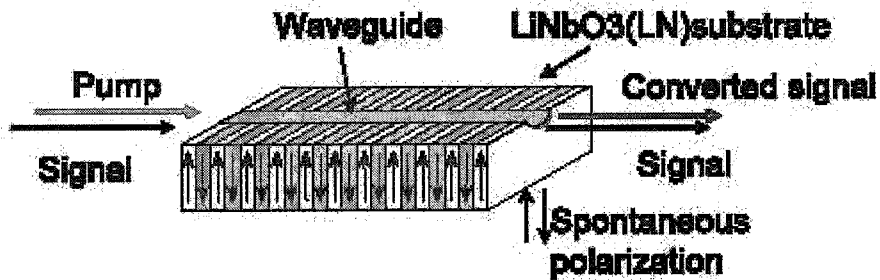


Fig.1.5 device structure of QPM-LN wavelength converter [6]

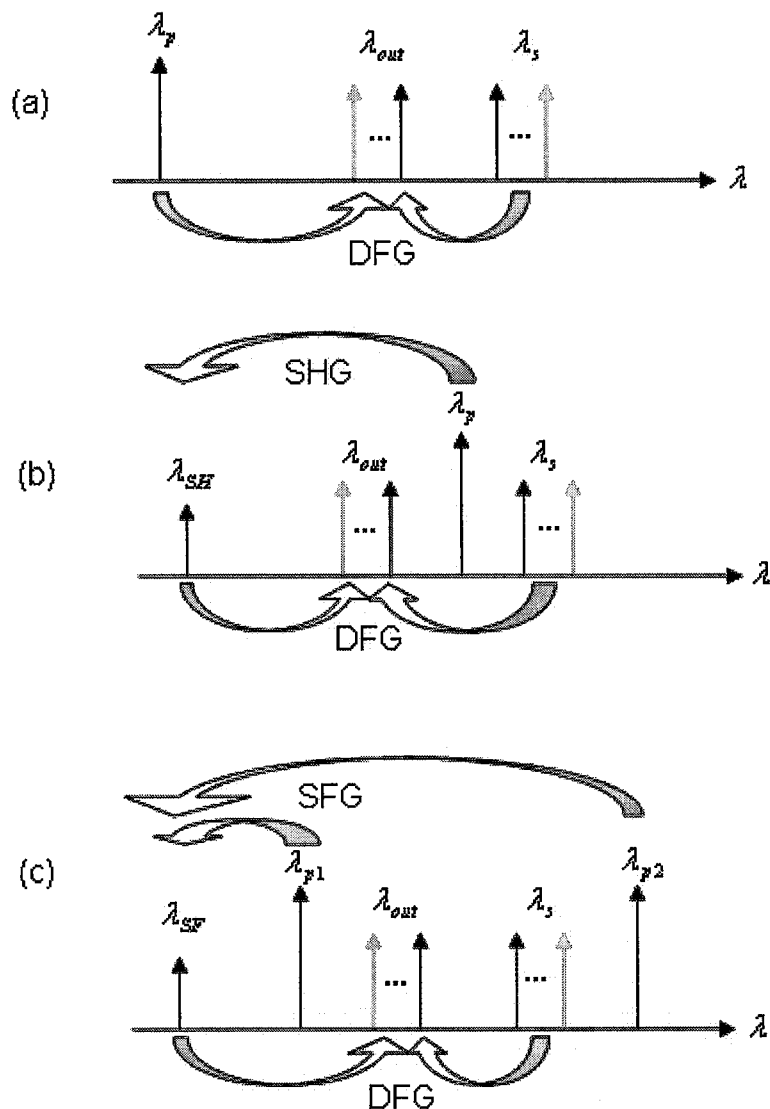


Fig.1.6 schematic diagram of a) direct DFG, b) cascaded SHG: DFG, c) cascaded SFG: DFG. In SFG:DFG scheme, SFG process takes place between two pump or one pump and the signal.

In DFG based wavelength conversion, it is difficult to simultaneously launch the pump in the 770nm band and the signal in the 1550nm band into the fundamental mode of waveguide. The cascaded SHG:DFG and cascaded SFG:DFG based wavelength conversion overcomes this problem, where signal and pump waves are in the same 1550nm band. In cascaded SHG:DFG scheme, the 1550nm band pump at frequency ω_p first generates a second-harmonic wave at frequency $\omega_{SH} = 2\omega_p$, then the latter play a role of the pump source in the successive DFG process and generate the desired converted wave at frequency $\omega_c = \omega_{SH} - \omega_s = 2\omega_p - \omega_s$. Since a strong pump wave is located in the communication band, the SHG:DFG scheme may not be acceptable in some applications. The cascaded SFG:DFG based wavelength conversion has the advantage of no pump occupation. In this case, two 1550nm band pump waves at frequencies ω_{p1} and ω_{p2} , which are set out of the communication band, first generates a sum frequency wave at frequency $\omega_{SF} = \omega_{p1} + \omega_{p2}$. Then in the successive DFG process, this SF wave interacts with the signal wave at frequency ω_s and generates the desired converted wave at frequency $\omega_c = \omega_{SF} - \omega_s = \omega_{p1} + \omega_{p2} - \omega_s$. The cascaded SHG:DFG and cascaded SFG:DFG scheme include two successive second-order nonlinear processes, so the conversion efficiency is much less than DFG scheme.

However, the disadvantage of DFG scheme may be overcome by using an integrated coupling structure, which have been introduced by Chou, et al. [7]. Chou proposed this structure on a pure lithium niobate device. However, pure lithium niobate is susceptible to photorefractive perturbations and restricts highly efficient wavelength conversion. Although this problem can be overcome by operating at high temperature ($\sim 120^\circ\text{C}$), it is a major concern for some commercial application of wavelength conversion devices. Doping lithium niobate with MgO has been found to greatly reduce photorefractive sensitivity. [8] To allow the device to work at room temperature and improve the conversion efficiency, an integrated coupling structure on a MgO doped lithium niobate wavelength converter is studied and implemented in this thesis. The wavelength converter in this work is designed to convert wavelength from the C-band to the L-band, which is able to improve communication capacity.

1.4 Overview

The research described in this thesis involves the development of wavelength conversion devices based on quasi-phase-matched MgO doped lithium niobate waveguide. This thesis starts from understanding the physics of DFG wavelength conversion and waveguide. Then, based on the understanding of QPM and PPLN waveguide fabrication, an integrated coupling structure is designed and implemented, which allows for robust coupling of the interacting

waves and essential for improvement of device performance such as conversion efficiency. The performance of integrated coupling structure and the combined conversion device are tested.

The organization of this thesis is summarized as follows. Chapter 2 derives the coupled mode equations for the DFG process and discussed the operating principle of waveguide. Chapter 3 describes the fabrication and modeling of APE PPLN waveguides. Chapter 4 describes the integrated waveguide structures for wavelength conversion. Chapter 5 shows the performance of the wavelength conversion device with the integrated coupling structure. Finally, chapter 8 concludes this thesis.

Chapter 2

Theory of guided-wave quasi-phase matched wavelength conversion

This chapter summarizes the basic theory of quasi-phase matched (QPM) wavelength conversion in waveguides. Nonlinear processes of DFG and SHG are described. Maxwell's equations, a complete description of the production and interaction of electric and magnetic fields, are used to derive a set of coupled differential equations describing the interaction of optical waves. Solutions for second harmonic generation and difference frequency generation are presented, which is utilized for numerical analysis of the nonlinear processes. The QPM technique is described and discussed. Basic waveguide theory is also presented.

2.1 Difference Frequency Generation and Second Harmonic Generation (DFG & SHG)

The Wavelength converter developed in this work is based on difference frequency generation (DFG) in second-order nonlinear material. In an optical material system, dielectric polarization, defined as dipole moment per unit volume, is induced by an optical electric field. The polarization P is approximately proportional to the electric field E for the cases of small field amplitude.

$$P^L = P^{(1)} = \epsilon_0 \chi^{(1)} E \quad (2.1)$$

Where P^L is the linear polarization, ϵ_0 is the permittivity of free space.

While at the presence of a sufficiently intense laser light in a nonlinear material system, induced nonlinear polarization P^{NL} becomes significant and can be expressed as a power series of E in (2.2)

$$P^{NL} = P^{(2)} + P^{(3)} + \dots = \epsilon_0 (\chi^{(2)} E^2 + \chi^{(3)} E^3 + \dots) \quad (2.2)$$

where $P^{(q)}$ and $\chi^{(q)}$ ($q \geq 2$) denote the nonlinear polarization and the nonlinear susceptibility of the q th order, respectively.

The nonlinear polarization acts as source of new frequency components of the electromagnetic field. For example, the second-order nonlinear susceptibility $\chi^{(2)}$, which requires crystal in the absence of inversion symmetric, gives rise to three-wave mixing interaction including second-harmonic generation (SHG), sum-frequency generation (SFG), difference-frequency generation (DFG), optical parametric oscillation (OPO).

SHG, also called frequency doubling, is the simplest three-wave mixing interaction. It is illustrated schematically in Fig.2.1. Here in a) of Fig.2.1, the incident radiation at frequency ω is converted to radiation at the second-harmonic frequency 2ω . In b) of Fig. 2.1, two photons of frequency ω are destroyed and a photon of frequency 2ω is simultaneously created in a single quantum-mechanical process. The solid line and dashed line represent the atomic ground state and virtual levels, respectively.

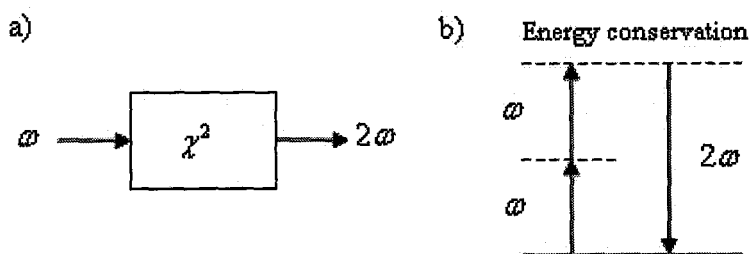


Fig.2.1 a) Geometry of second harmonic generation. b) Energy-level diagram describing second-harmonic generation

It is one of the most useful and commonly exploited nonlinear optical processes. One common use of SHG is to convert the output of a fixed frequency laser to a different spectral region. For example, the Nd:YAG laser operates in the near infrared at a wavelength of $1.06 \mu\text{m}$. SHG convert the wavelength of the radiation to $0.53 \mu\text{m}$, in the middle of the visible spectrum.

Consider the case of DFG, or called parametric down-conversion, a strong pump laser light at frequency ω_p (wavelength $\lambda_p = 2\pi c / \omega_p$) is mixed with a weak signal laser light at frequency ω_s (wavelength $\lambda_s = 2\pi c / \omega_s$), and a frequency-shifted output $\omega_{out} = \omega_p - \omega_s$ (wavelength $\lambda_{out} = 2\pi c / \omega_{out}$) is generated. Fig.2.2 a), b), and c) show schematic description, energy diagram and typical arrangement of DFG, respectively. The instantaneous nature of the parametric process allows for high speed operation of the wavelength converter devices.

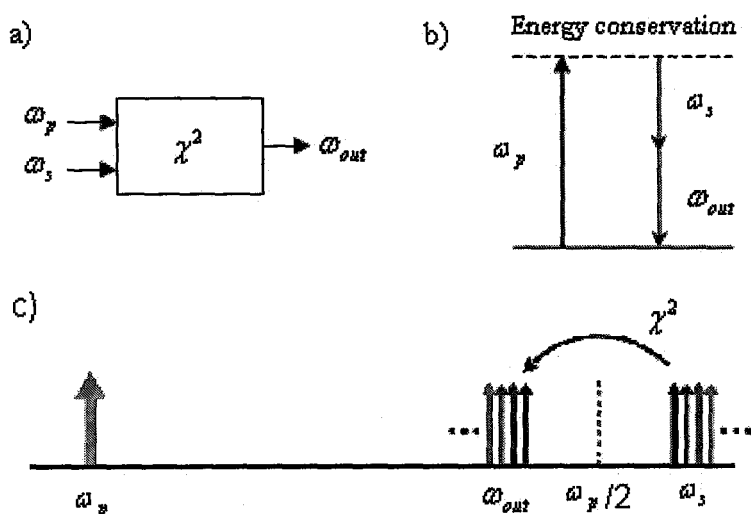


Fig.2.2 Schematic descriptions of difference-frequency generation between a pump at ω_p and a signal at ω_s .

When the pump frequency is close to twice of the signal frequency (which was called near-degenerate pump frequency), and write $\omega_s = \omega_p / 2 + \Delta$, then the output is at $\omega_{out} = \omega_p / 2 - \Delta$, i.e., the output is the mirror image of the signal frequency around the degenerate point. With a pump in the vicinity of 780 nm, signals in conventional band (C-band: 1530 - 1560 nm) can be converted to output with long wavelengths in the long-wavelength band (L-band: 1565 nm - 1625 nm).

2.2 Maxwell's Equations

The theory of three-wave mixing interaction can be described by Maxwell's equations [9].

$$\nabla \times \tilde{\mathbf{E}} = -\frac{\partial \tilde{\mathbf{B}}}{\partial t}, \quad (2.3 \text{ a})$$

$$\nabla \times \tilde{\mathbf{H}} = \tilde{\mathbf{J}} + \frac{\partial \tilde{\mathbf{D}}}{\partial t}, \quad (2.3 \text{ b})$$

$$\nabla \cdot \tilde{\mathbf{D}} = \rho, \quad (2.3 \text{ c})$$

$$\nabla \cdot \tilde{\mathbf{B}} = 0. \quad (2.3 \text{ d})$$

where $\tilde{\mathbf{E}}$ is the electric field, $\tilde{\mathbf{D}}$ is the electric displacement, $\tilde{\mathbf{B}}$ is the magnetic flux density, $\tilde{\mathbf{H}}$ is the magnetic field, $\tilde{\mathbf{J}}$ is the free current density. The device in this work contains no free charges, so that

$$\rho = 0, \quad (2.4)$$

Assume the material is lossless, so that

$$\tilde{\mathbf{J}} = 0. \quad (2.5)$$

The material in this work is non-magnetic, so that

$$\tilde{\mathbf{B}} = \mu \tilde{\mathbf{H}} = \mu_0 \tilde{\mathbf{H}}, \quad (2.6)$$

where μ is permeability of material, μ_0 is the permeability of free space. When consider the nonlinear polarization,

$$\tilde{\mathbf{D}} = \varepsilon \cdot \tilde{\mathbf{E}} = \varepsilon_0 \varepsilon_r \cdot \tilde{\mathbf{E}} + \tilde{\mathbf{P}}^{NL}, \quad (2.7)$$

where ε is the permittivity, ε_0 is the permittivity of free space, ε_r is the relative permittivity. The first term and the second term of the right side of (2.7) is linear and nonlinear polarization, respectively.

Derived from the Maxwell's equation above, the inhomogeneous optical wave equation under the slowly varying amplitude approximation is as follows:

$$-\nabla^2 \tilde{\mathbf{E}} + \mu_0 \varepsilon \cdot \frac{\partial^2 \tilde{\mathbf{E}}}{\partial t^2} = -\mu_0 \frac{\partial^2 \tilde{\mathbf{P}}^{NL}}{\partial t^2} \quad (2.8)$$

Consider each frequency component of the electric field and nonlinear polarization separately,

$$\tilde{\mathbf{E}}(r, t) = \sum_n [\mathbf{A}_n e^{-i(\omega_n t - k_n r)} + c.c.], \quad (2.9)$$

$$\tilde{\mathbf{P}}^{\text{NL}}(r, t) = \sum_n [\mathbf{P}_n^{\text{NL}}(r) e^{-i(\omega_n t - k_n r)} + c.c.], \quad (2.10)$$

where the summation is to be taken over positive frequencies only, and \mathbf{A}_n is the spatially slowly varying amplitude of the electric field compared to $e^{ik_n r}$. Substituting (2.9) and (2.10) into (2.8), the wave equation can be obtained as:

$$-\nabla^2 \mathbf{A}_n + \mu_0 \omega_n^2 \varepsilon \cdot \mathbf{A}_n = -\mu_0 \omega_n^2 \mathbf{P}_n^{\text{NL}}, \quad (2.11)$$

2.3 Coupled-mode equation

In a second-order nonlinear process, we are interested only in the second-order polarization, which is given by:

$$\tilde{\mathbf{P}}^{(2)} = \varepsilon_0 \chi^{(2)} \tilde{\mathbf{E}}^2 = \varepsilon_0 2d \tilde{\mathbf{E}}^2 \quad (2.12)$$

where the nonlinear coefficient d defined as

$$d = \chi^{(2)} / 2 \quad (2.13)$$

In the SHG process, the component of the second order polarization is given by:

$$P_p^{(2)} = 2d\varepsilon_0 E_{SH} E_p^* \quad (2.14.a)$$

$$P_{SH}^{(2)} = d\varepsilon_0 E_p^2 \quad (2.14.b)$$

In the DFG process, the component of the second order nonlinear polarization can be expressed as:

$$P_p^{(2)} = 2d\varepsilon_0 E_s E_{out} \quad (2.15.a)$$

$$P_s^{(2)} = 2d\varepsilon_0 E_p E_{out}^* \quad (2.15.b)$$

$$P_{out}^{(2)} = 2d\varepsilon_0 E_p E_s^* \quad (2.15.c)$$

Substituting (2.10) into (2.11) yields the following set of coupled mode equations for SHG:

$$\frac{dA_p}{dx} = -j2\omega_p \kappa^* A_p^*(x) A_{SH} \exp(-j\Delta kx) - \frac{\alpha_p}{2} A_p \quad (2.16.a)$$

$$\frac{dA_{SH}}{dx} = -j\omega_{SH} \kappa A_p(x) A_p \exp(j\Delta kx) - \frac{\alpha_{SH}}{2} A_{SH} \quad (2.16.b)$$

where the phase velocity mismatch due to material dispersion is :

$$\Delta k = k_p - 2k_{SH} \quad (2.17)$$

and $k_i = 2\pi n_i / \lambda_i$ is the propagation constant at the corresponding frequency, $i = p, SH$, λ_i is wavelength in vacuum, n_i is refractive index at that wavelength.

The constant κ is defined as

$$\kappa = \varepsilon_0 d_{\text{eff}} \sqrt{\frac{1}{2n_e(\lambda_{SH})n_e^2(\lambda_p)A_{\text{eff}} \left(\frac{\mu_0}{\varepsilon_0}\right)^{3/2}}} \quad (2.18)$$

The effective area A_{eff} equals the inverse square of the overlap integral among the modes of the interacting waves ($A_{eff} = \nu^{-2}$), which is defined as:

$$\nu = \int_{-\infty}^{\infty} \int_{-\infty}^{\infty} d(x, y) E_{SH}^2(x, y) E_p^*(x, y) dx dy \quad (2.19)$$

where $d(x, y)$ is transverse profile of the normalized nonlinearity.

α_i ($i = p, SH$) is the propagation loss of the material, including scattering and absorption losses.

For the case of DFG, the coupling equation is as follows[10]:

$$\frac{dA_p}{dz} = -j\omega_p \kappa A_s(z) A_{out}(z) \exp(j\Delta kz) - \frac{\alpha_p}{2} A_p \quad (2.20.a)$$

$$\frac{dA_s}{dz} = -j\omega_s \kappa^* A_{out}^*(z) A_p(z) \exp(-j\Delta kz) - \frac{\alpha_s}{2} A_s \quad (2.20.b)$$

$$\frac{dA_{out}}{dz} = -j\omega_{out} \kappa^* A_s^*(z) A_p(z) \exp(-j\Delta kz) - \frac{\alpha_{out}}{2} A_{out} \quad (2.20.c)$$

Where the phase velocity mismatch due to material dispersion is :

$$\Delta k = k_p - k_s - k_{out} \quad (2.21)$$

and $k_i = 2\pi n_i / \lambda_i$ is the propagation constant at the corresponding frequency, $i = p, s$, or out , λ_i is wavelength in vacuum, n_i is refractive index at that wavelength. The constant κ is defined as

$$\kappa = \epsilon_0 d_{eff} \sqrt{\frac{1}{2n_e(\lambda_p) n_e(\lambda_s) n_e(\lambda_{out}) A_{eff}} \left(\frac{\mu_0}{\epsilon_0} \right)^{3/2}} \quad (2.22)$$

And the effective area A_{eff} is defined as

$$A_{eff} = 1 / \nu^2 \quad (2.23)$$

where ν is overlap integral and defined as

$$\nu = \int_{-\infty}^{\infty} \int_{-\infty}^{\infty} d(x, y) E_s(x, y) E_{out}(x, y) E_p^*(x, y) dx dy \quad (2.24)$$

The coupling equation for cascade SHG:DFG is as follows [11]:

$$\frac{dA_p}{dz} = -j\omega_p \kappa_{SHG}^* A_p(z) A_h(z) \quad (2.25.a)$$

$$\frac{dA_h}{dz} = -j\omega_p \kappa_{SHG} A_p^2(z) - j\omega_h \kappa_{DFG}^* A_{out}(z) A_s(z) \exp(j\Delta kz) \quad (2.25.b)$$

$$\frac{dA_s}{dz} = -j\omega_s \kappa_{DFG} A_{out}^*(z) A_h(z) \exp(-j\Delta kz) \quad (2.25.c)$$

$$\frac{dA_{out}}{dz} = -j\omega_{out} \kappa_{DFG} A_s^*(z) A_h(z) \exp(-j\Delta kz) \quad (2.25.d)$$

where A_p , A_h , A_s and A_{out} are power normalized amplitudes of the pump, harmonic, signal, and difference frequency waves, respectively, κ_{SHG} and κ_{DFG} are the

coupling coefficients for SHG and DFG, $\kappa_{SHG} \approx \kappa_{DFG}$ for $\omega_{out} \approx \omega_s$, the phase velocity mismatch due to material dispersion is :

$$\Delta k = k_h - k_s - k_{out} \quad (2.26)$$

and $k_i = 2\pi n_i / \lambda_i$ is the propagation constant at the corresponding frequency, $i = h, s$, or out, λ_i is wavelength in vacuum, n_i is refractive index at that wavelength.

Solutions

There are several solutions of the coupled equations under different assumption. In the case of SHG process, lossless material $\alpha_p = \alpha_{SH} = 0$ is considered and the initial condition $A_p(0) = A_{p0}$ and $A_{SH}(0) = 0$ is assumed, where A_{p0} is the amplitude of the incident pump light is. If the interaction is weak, therefore there is a very small depletion of the pump wave power and low gain of the input signal, we can approximate $A_p(z)$ and $A_s(z)$ as $A_p(z) = A_{p0}$ and $A_s(z) = A_{s0}$. In the no pump depletion approximation (NDPA), the coupled-mode equation can readily be integrated to be

$$A_{SH}(z) = -j\kappa A_{p0}^2 z \exp(j\Delta kz / 2) \left(\frac{\sin \Delta kz / 2}{\Delta kz / 2} \right) \quad (2.27)$$

and the conversion efficiency is defined as

$$\eta = \frac{|A_{SH}(L)|^2}{|A_p(0)|^2} = \kappa^2 P_p L^2 \left(\frac{\sin(\Delta kL / 2)}{\Delta kL / 2} \right)^2 \quad (2.28)$$

where $P_p = A_{p0}^2$ is the incident pump power. The normalized conversion efficiency η_{nor} ($\% \cdot W^{-1} cm^{-2}$), a commonly used parameter to represent the conversion performance, is given by

$$\eta_{nor} = \frac{P_{SH}}{P_p^2 L^2} = \kappa^2 = \frac{\epsilon_0^2 d_{eff}^2}{2n_e^2(\lambda_p)n_e(\lambda_{SH})A_{eff}} \left(\frac{\mu_0}{\epsilon_0} \right)^{3/2} = \frac{\eta}{P_p L^2} \quad (2.29)$$

It is independent of device length and input power, and depends on the nonlinear properties of the medium and the overlap of the interacting waves.

For the case of DFG process, consider lossless material ($\alpha_p = \alpha_s = \alpha_{out} = 0$) and assume the initial condition $A_p(0) = A_{p0}$, $A_s(0) = 0$ and $A_{out}(0) = 0$, the coupled equation is integrated to be,

$$A_{out}(z) = -j\kappa A_{p0} A_{s0}^* z \exp(j\Delta kz / 2) \left(\frac{\sin(\Delta kz / 2)}{\Delta kz / 2} \right) \quad (2.30)$$

Note that the output is proportional to the complex conjugate of the signal, so that the wavelength converter based on DFG can function as a spectral inverter.

The conversion efficiency is

$$\eta = \frac{|A_{out}(L)|^2}{|A_s(0)|^2} = \kappa^2 P_p L^2 \left(\frac{\sin(\Delta k L / 2)}{\Delta k L / 2} \right)^2 \quad (2.31)$$

And the normalized efficiency ($\% \cdot W^{-1} cm^{-2}$) is

$$\eta_{nor} = \frac{P_{out}}{P_p P_s L^2} = \kappa^2 = \frac{\epsilon_0^2 d_{eff}^2}{2n_e(\lambda_p)n_e(\lambda_s)n_e(\lambda_{out})A_{eff}} \left(\frac{\mu_0}{\epsilon_0} \right)^{3/2} \quad (2.32)$$

For near-degenerate case, where the pump frequency is close to twice of the signal frequency, the value of normalized DFG efficiency is approximately equal to that of normalized SHG efficiency.

In equation (2.20) and (2.25), for $\Delta k = 0$, the efficiency under the QPM condition is

$$\eta = \eta_{max} = \kappa^2 P_p L^2 \quad (2.33)$$

The conversion efficiency in (2.20) and (2.25) becomes [6]

$$\eta_L = \eta_{max} \frac{\sin(\Delta k L / 2)}{\Delta k L / 2} = \eta_{max} \text{sinc}^2(\Delta k L / 2) \quad (2.34)$$

The phase mismatch factor $\text{sinc}^2(\Delta k L / 2)$ is shown in Fig.2.3. At the presence of nonzero phase-mismatch, the conversion efficiency decreases with some oscillations as $|\Delta k|L$ increases. Along a certain propagation distance L_{coh} , the relative phase mismatch of interacting waves reaches π , the conversion efficiency reaches zero and the power of generated wave starts to flow back into the pump wave. The coherence length of the interaction L_{coh} is defined as

$$L_{coh} = \pi / \Delta k \quad (2.35)$$

In general, a practical intensity of the generated wave can never be obtained.

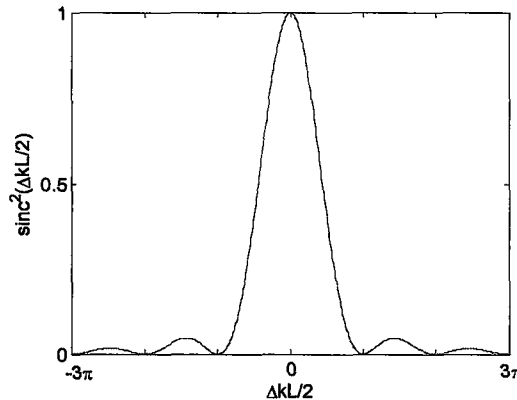


Fig.2.3. Effects of phase mismatch on the conversion efficiency

2.4 Quasi Phase Matching (QPM)

To keep a positive net power flow to generated wave and achieve highly efficient conversion, it is essential to satisfy the phase matching condition. Rather than perfect phase matching, the quasi-phase matching (QPM) method has been

proved to be more effective in most practical devices. In QPM structures, the nonlinear coefficient of the material along the propagation axis is modulated with period Λ to compensate for the phase mismatch of the interacting waves with different wavelengths, the value of which Δk satisfies the following equation.

$$\Delta k = |k_p - k_s - k_{out}| = \frac{2m\pi}{\Lambda}, \quad (2.36)$$

where $k_i = 2\pi n_i / \lambda_i$ ($i = p, s, \text{ or } out$; λ_i is wavelength in vacuum, n_i is refractive index at that wavelength. m stands for the m th order QPM condition.

The nature of the compensation effect is illustrated in Fig.2.4 B1 and B3 below. Here it is assumed that the period Λ of the alternation of the crystalline axis has been set equal to twice the coherent length L_{coh} of the nonlinear interaction. Then, each time the field amplitude of the generated wave is about to begin to decrease as a consequence of the phase mismatch, a reversal of the sign of polarization occurs which allows the field amplitude to continue to grow monotonically. While in Fig.2.4 A for exact phase matching, the efficiency increase monotonically, and in Fig.2.4 C for no phase matching, the efficiency oscillates periodically.

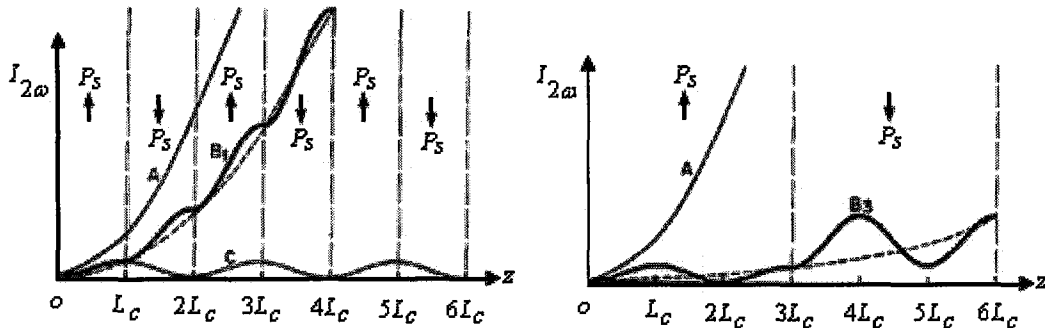


Fig.2.4: Diagram of quasi-phase matching plotting the second harmonic signal for the conditions of: A. Perfect phase matching, C. No phase matching, B1. First-order QPM, and B3. Third-order QPM [12].

QPM technique offer many advantages over other phase matching techniques. First, wavelength conversion between various wavelengths from the ultraviolet to the near infrared in the transparent range of the crystal can be achieved simply by choosing a suitable inversion period in the QPM structure. While only interactions at certain wavelengths could be phase-matched for angle phase matching technique. Second, the propagating waves can undergo the largest nonlinear interaction in the crystal, enhancing the conversion efficiency. For instance, the largest nonlinear tensor component of lithium niobate (d_{33}) enabling QPM is approximately six times larger than the one (d_{31}) enabling birefringent phase matching. Additionally, Tuning behaviour can be engineered through aperiodic QPM grating.

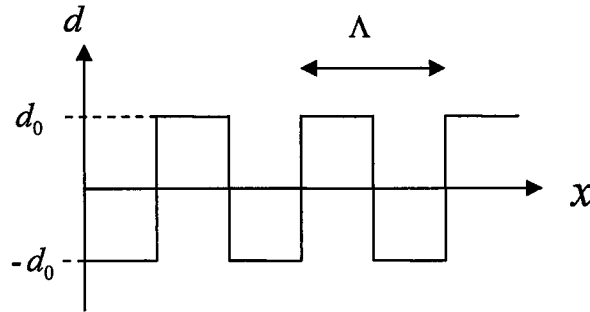


Fig.2.5 Square-shaped modulation of the nonlinear coefficient $d(x)$ for quasi-phase matching

The mathematical description of QPM can be formulated as follows [12]. Let $d(x)$ denote the spatial dependence of the nonlinear coupling coefficient. One of the most efficient types of QPM shown in Fig.2.5 is periodic and abrupt sign change of nonlinear coefficient, and $d(x)$ is simply the square-wave function with period of Λ along the propagation and can be represented as

$$d(x) = d_0 \text{sign}[\cos(2\pi x / \Lambda)], \quad (2.37)$$

where d_0 denotes the nonlinear coefficient of the homogeneous material. Here the duty cycle $D = \frac{l}{\Lambda} = 50\%$ is the same as example shown in Fig.4 B, where l is the length of reversed domain, Λ is the period of domain reversal. The nonlinear optical coefficient of d_{33} is utilized in most QPM-LN waveguide devices. More complicated spatial variations are also possible. It is useful to describe the spatial variation of $d(x)$ in terms of a Fourier series as

$$d(x) = d_0 \sum_{m=-\infty}^{m=\infty} G_m \exp(ik_m x), \quad (2.38)$$

where $k_m = 2\pi m / \Lambda$ is the grating vector associated with the m th Fourier component of $d(x)$. For the modulation in the form of square function as in the example above, the coefficients G_m are readily shown to be given by

$$G_m = (2 / m\pi) \sin(m\pi / 2), \quad (2.39)$$

Note that in coupled equations (2.12), one assumes that one particular Fourier component of $d(x)$ provides the dominant coupling among the interacting waves. The effective nonlinear coupling coefficient depends on the Fourier order m according to

$$d_{\text{eff}} = d_0 G_m \quad (2.40)$$

In general, the higher the order m , the lower value the coefficient d_{eff} and the lower value the conversion efficiency. For the first order QPM (where $m=1$), the optimum duty cycle is $D = 50\%$,

$$G_1 = \frac{2}{\pi}, \quad (2.41)$$

so that

$$d_{eff} = \frac{2}{\pi} d_0 \quad (2.42)$$

The optimum period for the first order QPM structure is

$$\Lambda_1 = 2L_{coh} = \frac{2\pi}{\Delta k} \quad (2.43)$$

The period for the m th order QPM satisfy:

$$\Lambda_m = m\Lambda_1 \quad (2.44)$$

Using the corresponding Sellmeier equation for the refractive index of different crystal, it is possible to calculate the required period as a function of the wavelength of the interacting waves. The practical range of QPM periods for SHG with radiation at a wavelength of $900 \sim 1600 \text{ nm}$ is roughly $4 \sim 20 \mu\text{m}$.

Consider the first order QPM condition including slight phase mismatch, the coupled-mode equation is identical to (2.16) and (2.20) [13], but the phase mismatch is replaced as

$$\Delta k' = k_p - k_s - k_{out} - \frac{2\pi}{\Lambda} \quad (2.45)$$

which represents the deviation from the quasi-phase matching condition, and the effective nonlinear coefficient is replaced as

$$d_{eff} = \frac{2}{\pi} d_0 \quad (2.46)$$

2.5 Waveguide

Waveguide geometry allows an increase in conversion efficiency by several orders of magnitude as compared to bulk media, due to tight modal confinement of the interacting waves over entire interaction distances, rather than simply near the focal point of a lens used for bulk configuration. Consequently, it provides a means to control precisely the spatial characteristics of generated waves.

The basic waveguide structure of slab waveguide is shown in Fig.2.6, together with the index profiles of step-index type waveguide and graded-index type waveguide along the depth. The indices of the cladding layer, guiding layer, and substrate are n_c , n_f and n_s , respectively.

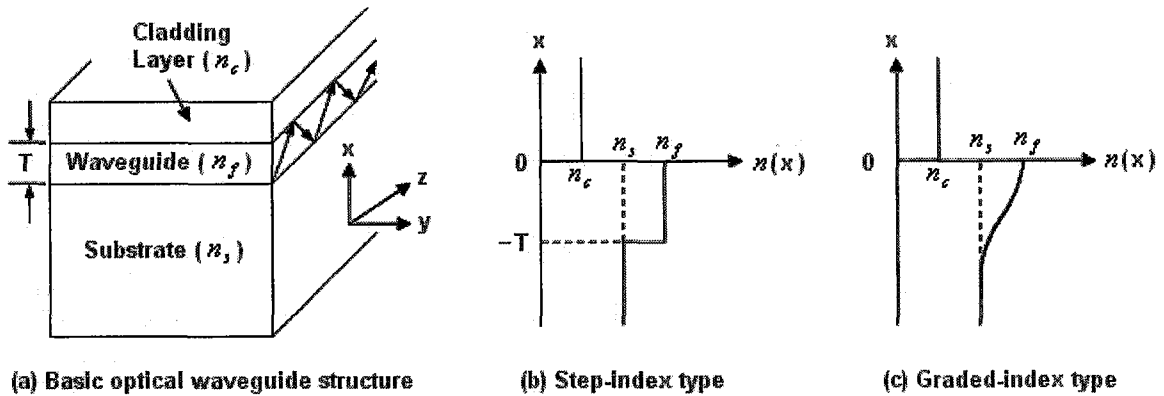


Fig.2.6 slab optical waveguide: a) basic structure, b) index profile of step-index type, and c) graded-index type[14]

Mode propagation characteristics of waveguide can be analyzed by ray-optics, which takes into account the total internal reflection at the interfaces and the accompanied phase shifts. Consider an incident coherent light at an angle θ between the wave normal and the normal to the interface in the step-index slab waveguide. The critical angles at both upper and lower interfaces, are respectively

$$\theta_c = \sin^{-1}(n_c / n_f) \tag{2.47}$$

And

$$\theta_s = \sin^{-1}(n_s / n_f) \tag{2.48}$$

In general, $n_f > n_s > n_c$, so $\theta_s > \theta_c$. Three possible ranges of the incident angle θ presents three modes of waveguide: a) $\theta_s < \theta < 90^\circ$, guided mode, b) $\theta_c < \theta < \theta_s$, substrate radiation mode, and c) $\theta < \theta_c$, substrate-clad radiation mode. The three different zig-zag ray-optical pictures are shown in Fig.2.7. The most important mode is guided mode. In this case, light is confined in the guiding layer by the total internal reflections at both upper and lower interfaces and propagates along the zig-zag path in Fig. 2.7(a). If the waveguide material is lossless, the light can propagate without attenuation. In substrate radiation mode, the light is totally reflected at the upper interface while escapes from the guiding layer thorough the cover, according to Snell's law for $\theta < \theta_s$. The amplitude of light decreases significantly along the propagation direction. In substrate-clad radiation mode, light escapes both from the cover and the substrate.

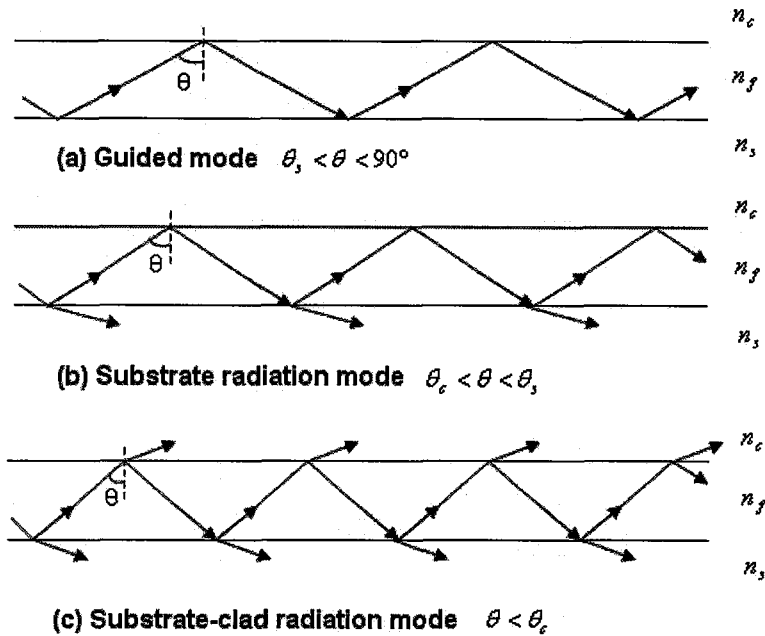


Fig.2.7 Zig-zag propagating path of light along optical waveguides for different modes [14]

The analytical results in ray optics are consistent with the derived results based on wave optics. In wave optics, modes are generally characterized by propagation constants. The plane wave propagation constant in the wave-normal direction is defined as $k_o n_f$, where $k_o = 2\pi/\lambda$ and λ is the wavelength in vacuum. Wave-vector diagram is shown in Fig.2.8, where $k_x = k_o n_f \cos \theta$ and $k_z = k_o n_f \sin \theta = \beta$. Here, β is equivalent to the plane wave propagation constant in a medium with an effective index $N = n_f \sin \theta$, defined as $\beta = k_o N$. The range of N for guided mode propagating along the z direction is $n_s < N < n_f$.

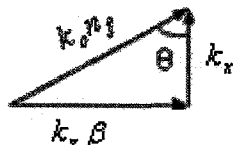


Fig.2.8 wave-vector diagram

In slab waveguide, the light confinement takes place in depth only, and the guided light width expands due to diffraction during propagation. In channel waveguide, light is effectively confined both in width and in depth. There are several different types of channel waveguide. Fig 2.9 shows two typical types as buried waveguide and ridge waveguide. In buried type, higher index guiding

layers are formed near the substrate surface. While in ridge type, the undesired higher-index film is removed from the substrate.



Fig.2.9 Typical structures of optical channel waveguides: a) buried type, b) ridge type. ($n_f > n_s$)

Buried waveguides have several features over ridge waveguide. First, the higher symmetry of their index profile in depth, with respect to that of surface waveguides, can yield a better modal overlap and help reduce coupling losses to and from optical fibers. Besides, propagation losses associated with scattering from surface defects or roughness can be significantly lowered in the embedded structured, compared to ridge waveguides. [15] Thus, buried waveguide is more suitable for optical waveguide devices.

In optical channel waveguides, pure TE and TM modes are not supported, and two families of hybrid modes exist. The hybrid modes supported by the channel modes polarized along the x and y directions. The guided modes supported by the channel waveguide are classified depending upon whether the main electric field component lies in the x or y direction. The mode having the main electric field E_x is called the E_{pq}^x mode or TM-like mode, which resembles the TM mode in a slab waveguide. The subscripts p and q denote the number of nodes of the electric field E_x in the x and y directions, respectively. Similarly, the E_{pq}^y mode or TE-like mode has the main electric field of E_y . It is not easy to calculate the radiation pattern from the channel waveguide analytically. An analytical method such as Marcatili's method does not give the accurate field distribution, especially for the cladding region. The accurate electromagnetic field distribution in the rectangular waveguide is determined numerically by the finite element method, beam propagation method, etc. In this work, we will simulate the waveguide by BPM-CAD software with will be discussed in Chapter. 3.

Chapter 3

Device fabrication and waveguide modeling

In order to demonstrate efficient wavelength converter device, suitable material with appropriate nonlinearity to achieve quasi-phase matching (QPM) technique and to fabricate homogeneous low-loss waveguides is required. In this work, periodically poled lithium niobate (LN) waveguide is fabricated by the periodic poling technique for QPM structure and the annealed proton-exchanged (APE) technique for waveguide.

In this chapter, LN as the substrate for wavelength converter will be briefly discussed. Then, the fabrication of QPM structure and waveguide in this work will be described. The refractive index profile model of waveguide and the Sellmeier equation describing the refractive index dispersion of LN are also provided.

3.1 lithium niobate (LN)

Among the commercial nonlinear optical materials, lithium niobate (LN) has been extensively employed to be the carrier of nonlinear optical devices, and was referred as “the silicon of nonlinear optics”. The choice of LN as the substrate of wavelength converter in this work is motivated by several factors.

First of all, to achieve efficient wavelength conversion in nonlinear optical processes, the nonlinear coefficient of the material is required to be as large as possible. The largest value of second order nonlinear tensor for LN d_{33} equals 25.0 pm/V at $\lambda=1064\text{nm}$ [16], which is the largest compare to any ferroelectric material. While some semiconductor materials (e.g. GaAs) provide significantly larger nonlinear coefficients, ferroelectric material has some significant advantages from fabrication point of view.

Secondly, the material must be transparent at all wavelengths involved in nonlinear processes. LN has wide transparent spectral window, with wavelength ranging from the band gap edge absorption at wavelength about 320 nm up to the first infrared vibrational absorptions at wavelength about 5 μm . Wavelengths of device concept and experiments in this work are ranging from near infrared to short-wavelength infrared (telecommunication spectral region). LN satisfies the spectral requirement completely.

Furthermore, from an industrial point of view, commercial availability and low cost are often considered. Large wafers of LN with diameter of three or four inch are readily available at a cost as low as \$ 150 per wafer for pure LN and \$ 400 for MgO:LN from several vendors all over the world, such as Yamaju Ceramics Co. Ltd. This crystalline dielectric material has good optical quality with a large degree of optical homogeneity as $\Delta n \sim 10^{-5}$.

Most importantly, fabrication techniques for QPM and waveguide structure in LN have been well established. QPM structure allows engineering the

nonlinear response of a given material by periodically or aperiodically inversion of nonlinear susceptibility. This is straightforward in ferroelectric materials by inversion of the ferroelectric domains. Waveguide achieves a higher confinement than bulk configuration and increase conversion efficiency for several orders. Details of the fabrication technique will be described in 3.2.

Moreover, LN is a uniaxial crystal with trigonal 3m symmetry, and has a large birefringence (n_o and n_e are 2.286 and 2.203 at 632.8 nm, respectively). It is chemically stable at room temperature, and quite insensitive to humid surroundings. It has large piezoelectric and electro-optic coefficients, which make it suitable for surface acoustic wave (SAW) filters as well as phase/amplitude modulators.

3.2 Fabrication of QPM waveguide devices

The proposed QPM waveguide device is fabricated on the z-cut, y-propagating lithium niobate substrate with thickness of 0.5 mm. Fig.3.1 shows the APE PPLN process in this work. The fabrication process can be divided into two independent processes: the generation QPM structure by periodically reversing the spontaneous polarization of the lithium niobate, and the formation of waveguide on the substrate by diffusion method. After finishing the fabrication process, the two ends of the substrate are polished for optical coupling at the input and output.

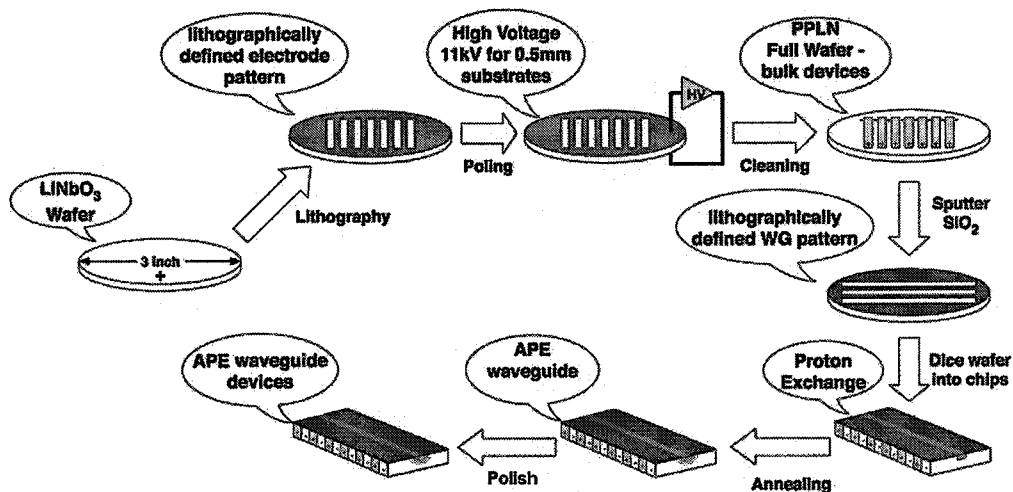


Fig.3.1 Device fabrication process chart [1]

The periodical ferroelectric domain inversion on a uniform z-cut LiNbO₃ wafer can be achieved in several ways, such as Ti-indiffusion [11], electric poling [11], direct bonding technique [17]. The most widely used method is electric poling, in which a high-voltage pulse is applied to electrodes lithographically patterned on the surface of the wafer. Domain reversals are induced in the area under the electrodes, so that simple periodic pattern can be fabricated. The

domain periods required for wavelength conversion in this work are $19.5 \mu\text{m}$, which is easier to fabricate compare to domain periods with several μm . Fig.3.2 shows a micrograph of PPLN surface with high poling quality.

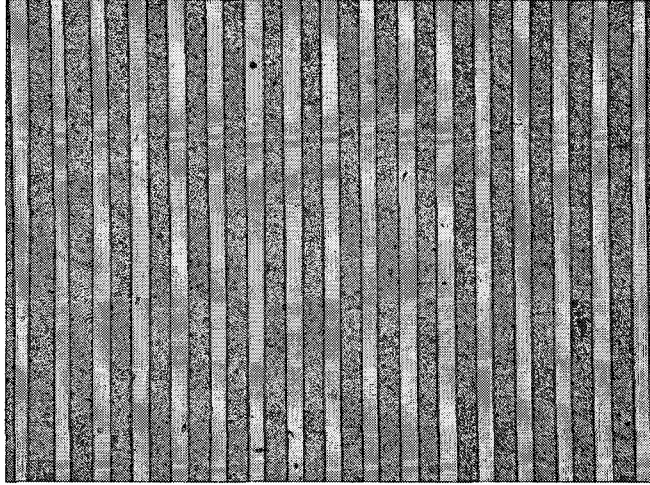
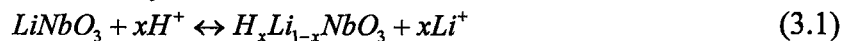


Fig.3.2 Micrograph of PPLN surface after etching in hydrofluoric acid. Domains of reserved polarity are etched, while original domains are not, such that domain boundaries are revealed as lines.

After electric-field poling, a piece of crystal is cut from a crystal wafer and cleaned for waveguide formation. There are several waveguide fabrication technique, such as Ti diffusion [18], annealed proton exchange (APE) [19-21], reverse proton-exchange (RPE) [22], mechanically fabricated or chemically etched ridge waveguide, etc. Among them, APE technique for LN waveguide has been well established and widely applied in fabrication of integrated optical devices, which was used to form waveguides in this work. APE process is an important technique for the fabrication of low-loss optical waveguides in LN. It includes two stages: proton-exchange (PE) process and annealing treatment.

The first step of PE process is optical lithography. In this step, a mask pattern with channel openings of a few micron widths along the crystallographic y -direction is formed on the $+z$ side of the LN wafer. Then, the substrate with the mask pattern is immersed in a weak acid such as pure benzoic acid and kept at a fixed temperature for a few hours. A number of hydrogen (H) atoms in the proton source are exchanged with Li^+ ions in the substrate through the mask opening which is left exposed to the acid attack, and a thin PE layer with composition of $H_xLi_{1-x}NbO_3$ (x : exchange ratio) is formed. The exchange reaction is approximately described by



In the PE layer, the extraordinary refractive index n_e is larger than that of the substrate, while the ordinary refractive index n_o is slightly smaller than that of the substrate.[23] Therefore, only light polarized along the crystal c axis will be

guided. In the case of z -cut LN, only transverse-magnetic (TM) modes is supported in PE waveguide. [11] PE process produces a waveguide with step-like refractive index profiles.

There are several different crystallographic phases depending on the proton concentration in PE waveguides [24], α phase for $x < 0.12$, $\alpha + \beta$ phase for $0.12 < x < 0.56$, and β phase for $0.56 < x < 0.8$, etc. The complex chemistry causes serious problems such as instability of waveguide parameters, enhanced propagation losses, and greatly reduced electrooptic and nonlinearity coefficient[25]. Therefore, second stage of annealing process phase is necessary to eliminate these problems.

After removal of the mask, the substrate is thermally annealed in a flowing dry oxygen gas for a few hours. Thermal annealing diffuses protons from the initial PE layer to a deeper region of the substrate, resulting in an extended graded index distribution and a reduction of the maximal index change. Well-annealed waveguides present only the α phase crystalline structure. The lattices constants of the α phase in $H_xLi_{1-x}NbO_3$ are approximately equal to those in substrate. While this diffusion reduces mode confinement and overlap (which determine efficiency), the annealing process restores the electrooptic coefficient, and reduces both the refractive index instabilities and the optical propagation losses. APE waveguides with a propagation loss of less than 1 dB/cm are obtained reproducibly for a wide wavelength range from visible to infrared.[11]

3.3 Modeling of refractive index profile for APE LN waveguide

Precise models of the wavelength-dependent refractive index profile are essential for the device design. In this section, an empirical analytical model for APE- $LiNbO_3$ channel waveguide is described. The model applies to z -cut APE- $LiNbO_3$ channel waveguide devices fabricated over a wide range of proton exchange and anneal processing conditions. The performances of APE- $LiNbO_3$ directional couplers, taper and bending waveguide have been analyzed using this model, with good agreement between the simulation and the experiment.

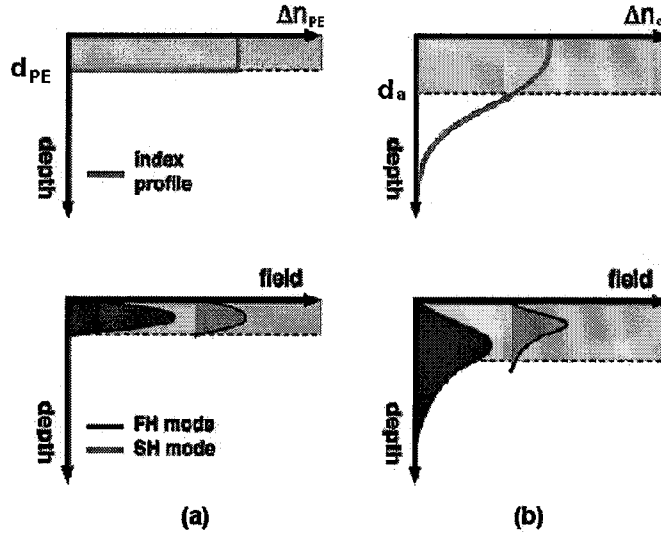


Fig.3.3 a) PE and b) APE index and mode profiles in the depth dimension. The gray layer represents the exchanged step index profile.[1]

The first stage of APE waveguide fabrication described in 3.3, proton exchange process, induces an approximately step-like rectangular refractive index profile shown in Fig.3.3 a), which characterized by a surface refractive index change (Δn_{PE}), an exchange depth (d_{PE}) and the exchange width w . The surface refractive index change Δn_{PE} is independent of exchange conditions, but is wavelength dependent [26].

$$\Delta n_{PE} = \sqrt{a_1 + \frac{a_2}{\lambda^2 - a_3}} \quad (3.2)$$

Where λ is wavelength in μm , the fitting values of the parameters $a_1 = 7.43 \times 10^{-3}$, $a_2 = 2.64 \times 10^{-3}$, $a_3 = 0.336$ for z -cut LiNbO_3 PE waveguide.

The depth d_{PE} depends on PE temperature T_{PE} and duration t_{PE} , and the relation is described by[11]

$$d_{PE} = 2\sqrt{D_{PE}(T_{PE})t_{PE}}, \quad (3.3)$$

$$D_{PE}(T_{PE}) = D_{PE0} \exp(-Q_{PE} / k_B T_{PE}), \quad (3.4)$$

Where $D_{PE}(T_{PE})$ is temperature dependent diffusion coefficient, k_B is the Boltzmann constant $8.617 \times 10^{-5} \text{ eV} \cdot \text{K}^{-1}$, D_{PE0} and Q_{PE} are diffusion constant and the activation energy with reported value of $5.04 \times 10^9 \mu\text{m}^2 \cdot \text{h}^{-1}$ and 1.030 eV for z -cut $\text{MgO}:\text{LiNbO}_3$ [27], respectively. The exchange width w is approximately the mask opening width in lithographical process.

Due to the different crystal phases involved in annealing process, the refractive index change of APE waveguide is not a linear function of the proton

concentration. Several analytical functions have been proposed. For simplicity, we are concerned with the behaviour of the refractive index change in the well annealed waveguide, which present only the α -phase crystalline structure and the proton concentration is smaller than 0.12. Moreover, the well annealed waveguide is generally used in electrooptic and nonlinear optic device applications, because of conserved value of nonlinear coefficient in low proton concentration.

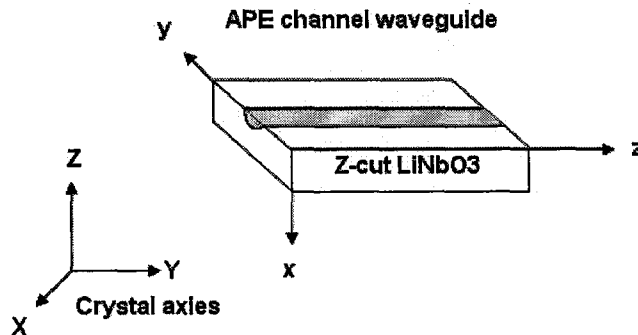


Fig.3.4 Coordinate system of the model and the crystal axes

We consider a y -propagating APE channel waveguide on a z -cut lithium niobate. In the coordinate system shown in Fig.3.4, z is the propagation direction and x is the depth direction.

Thermal annealing process forms the final waveguide with a graded refractive index profile $\Delta n_a(x, y)$ shown in Fig.3.3 b), which is a function of refractive index change (Δn_a) and a $1/e$ exchange depth (d_e).

The surface refractive index change (Δn_a) is given by [26].

$$\Delta n_a = \sqrt{a_1 + \frac{a_2}{\lambda^2 - a_3}} \quad (3.5)$$

where λ is wavelength in μm , the fitting values of the parameters $a_1 = 3.43 \times 10^{-5}$, $a_2 = 1.10 \times 10^{-5}$, $a_3 = 0.326$ for z -cut $LiNbO_3$ APE waveguide.

The proton concentration profile due to thermal annealing can be modeled as the solution of the following two dimensional diffusion equation, with diffusion in lateral and depth direction being independent and constant with respect to the diffusion time.

$$\frac{\partial C}{\partial t} = D_{ax}(T) \frac{\partial^2 C}{\partial x^2} + D_{ay}(T) \frac{\partial^2 C}{\partial y^2} \quad (3.6)$$

where C is the relative concentration distribution of the diffusing species, D_{ax} and D_{ay} are thermal annealing coefficients along the depth and width, respectively.

$$D_{ay}(T) = D_{ay0} \exp(-T_{y0}/T) \quad (3.7)$$

yields $D_{ay0} = 2.65 \times 10^{11} \mu m^2 \cdot h^{-1}$ and $T_{y0} = 1.67 \times 10^4 K$. [28]

$$D_{ax}(T) = D_{ax0} \exp(-T_{x0}/T) \quad (3.8)$$

yields $D_{ax0} = 8.62 \times 10^8 \mu\text{m}^2 \cdot \text{h}^{-1}$ and $T_{x0} = 1.28 \times 10^4 \text{K}$. [26] The initial condition is taken as the proton concentration distribution of PE process.

The solution to the diffusion equation for a finite source is given by

$$C(x, y) = \frac{\text{erf}\left(\frac{h/2 - x/2}{d_x}\right) + \text{erf}\left(\frac{h/2 + x/2}{d_x}\right)}{2\text{erf}\left(\frac{h}{2d_x}\right)} \cdot \frac{\text{erf}\left(\frac{w/2 - y}{d_y}\right) + \text{erf}\left(\frac{w/2 + y}{d_y}\right)}{2\text{erf}\left(\frac{w}{2d_y}\right)} \quad (3.9)$$

where h is the depth and w is the width of the initial proton exchanged region. $d_x(d_y)$ is the diffusion length in the vertical (horizontal) direction defined as

$$d_{x(y)} = 2\sqrt{D_{ax(ay)}(T_a)t_a} \quad (3.10)$$

where t_a is the diffusion time.

Fig.3.5 (a) shows the index distribution of $8 \mu\text{m}$ -wide waveguide cross section at wavelength of 1550nm generated by the APE waveguide model, and Fig.3.5 (b) is the simulation results of the fundamental mode profile.

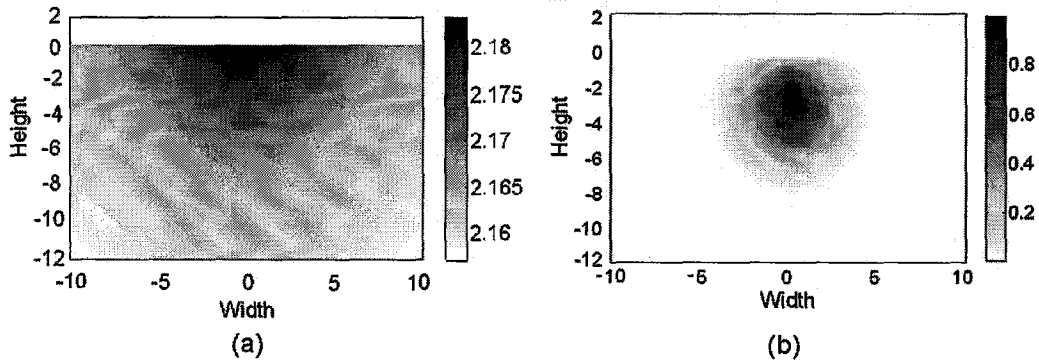


Fig.3.5 (a) index distribution of $8 \mu\text{m}$ -wide waveguide cross section, (b) simulation results of fundamental mode profile

3.4 Sellmeier equation:

For theoretically modelling, wavelength dependence of the refractive index is given by Sellmeier dispersion relation. Currently data for temperature-dependent dispersion of MgO-doped LiNbO_3 are rather scarce. In general, a Sellmeier equation for 5 mol % MgO-doped LiNbO_3 can be obtained by modifying the Sellmeier equation for congruent LiNbO_3 [29]. An improved temperature dependent Sellmeier equation for n_e in congruent LiNbO_3 was derived in Ref. [30] as

$$n_e^2 = a_1 + b_1 f + \frac{a_2 + b_2 f}{\lambda^2 - (a_3 + b_3 f)^2} + \frac{a_4 + b_4 f}{\lambda^2 - a_5^2} - a_6 \lambda^2 \quad (3.11)$$

where all the parameters a_i and b_i are given in Table 2, and the temperature parameter f related to crystal temperature T (unit in $^{\circ}\text{C}$) is given by

$$f = (T - 24.5)(T + 570.82) \quad (3.12)$$

Table 2 Parameters for Sellemier equation (3.11) [30]

Parameter	Value
a_1	5.35583
a_2	0.100473
a_3	0.20692
a_4	100
a_5	11.34927
a_6	1.5334×10^{-2}
b_1	4.629×10^{-7}
b_2	3.862×10^{-8}
b_3	-0.89×10^{-8}
b_4	2.657×10^{-5}

Temperature tuning curve of PPMgO:LN is calculated based on the above Sellmeier equation with a_1 as a fit parameter, the value of which is determined by least-squares fit to experimental tuning data shown in Fig. 5.5. The fitting method adjusts a_1 to minimize the sum given as

$$\sum_{n=1}^N (\lambda_n - \lambda_{fit})^2 \quad (3.13)$$

or minimize the standard deviation of QPM wavelength given as

$$\sqrt{\frac{1}{N} \sum_{n=1}^N (\lambda_n - \lambda_{fit})^2} \quad (3.14)$$

Here the sum runs over all N data points. λ_n is the experimental data of QPM wavelength, λ_{fit} is the numerically determined QPM wavelength by the fit parameter a_1 . With this method, a_1 was determined to be 5.47289, which is larger than the a_1 value of 5.35583 for congruent LiNbO_3 [30]. And the standard

deviation is around 7.7%, which implies that our modified Sellmeier coefficient allows accurate refractive-index predictions for n_e of MgO: $LiNbO_3$ in our case.

Chapter 4

Design of integrated coupling structure

4.1 Introduction

In DFG process, the wavelengths of signal and output wave are about twice that of the pump wave. It is very difficult to launch the pump into the fundamental mode of a waveguide that supports single mode at the signal and output wavelength, and hence several modes exist at pump wavelength, as shown in Fig.4.1.

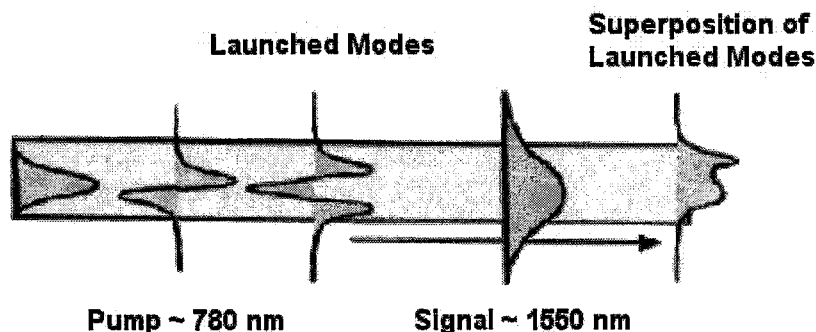


Fig.4.1 Schematic drawing of mode-launching issues. A single-mode waveguide for the signal wavelength supports multimodes for the pump wavelength. [3]

Due to the mode dispersion and QPM requirement, only one pump mode (usually the fundamental mode) contributes to the phase-matched DFG process. In the simple DFG device configuration, the signal and pump waves are coupled into the waveguide through a common optical fiber or coupling lens, it is difficult to couple pump wave and signal wave into the lowest order of the waveguide simultaneously with maximum coupling efficiency. As a result, a part of the incident pump power coupled to higher-order modes does not contribute to the conversion. It is desired that the signal and pump coupling can be optimized independently to accomplish maximum coupling to each fundamental mode.

An integrated coupling structure, refereed as integrated wavelength demultiplexer (WDM) in telecommunication, is a solution of the above problem. Chou, et al. [7] first propose this structure on a pure lithium niobate (LN) device. In this work, an integrated coupling structure is applied on a magnesium oxide (MgO) doped LN wavelength converter device.

LN with MgO doping is used for the following reason. The non-stoichiometry LN crystals present a large concentration of intrinsic defect. It bears several problems. Its high coercive field ~ 21 kV/mm limits the thickness of electric field poling (QPM fabrication technique in 3.2) to about 0.5 mm. Its low resistance to photorefractive damage (RPE) at room temperature limits the operating laser power density. Therefore, the material must be operated in an oven with a stable high temperature to increase its RPE threshold. Such a device is

inherently more complex and limits its application where heating is not expected. To overcome these disadvantages, MgO doping has been verified to be an effective method to eliminate the above drawbacks. MgO:LN has a coercive field of about 4.8 kV/mm, which is only about a quarter of LN's coercive field. It has been reported that the resistance of 5 mol% MgO:LN to photorefractive damage is enhanced up to 100 times higher than that of pure LN.[31] At the same time, MgO doping increases the conductivity of LN significantly, rendering the periodically poled MgO:LN (PPMgO:LN) to have a lower susceptibility to photorefractive damage, and making it possible to construct a reliable device in this material at room temperature.[8]

The integrated coupling structure can improve the conversion efficiency, as it allows for launching the input radiation into fundamental mode for nonlinear frequency conversion and allows for independent optimization of pump and signal input fiber-waveguide coupling. For these desires, integrate coupling structure includes the following components: mode filter which is designed to optimize the input fiber-waveguide coupling while keeping light propagating in fundamental mode, adiabatic taper which transform the mode size in different portions of the waveguides and allows coupling into the fundamental mode of multi-mode wavelength conversion waveguide, bends which accommodate the separation of input fibers, and directional coupler which combines the pump and signal into the wavelength conversion section.

In this Chapter, the theory and design of each on-chip components of the integrated coupling structure will be described separately. While optimizing the mode launching of fiber-waveguide and fundamental mode propagation of single mode waveguide to multi-mode waveguide, we also are concerned with the excess insertion loss and the length of the structure.

4.2 integrated coupling structure

A schematic structure of the device including both integrated coupling structure and DFG conversion section is shown in Fig.4.2. In addition to the straight waveguides, the proposed wavelength demultiplexing devices include two separate pump and signal wave coupling path. The coupler for the pump wave consists of a single-mode waveguide as a mode filter and an adiabatically tapered waveguide for smooth mode-size transformation. The signal wave is transmitted through a bent waveguide to change its optical path direction, and is coupled to the converter through a directional coupler. Fig.4.3 shows the micrograph of partial view of the integrated structure on periodic-poled lithium niobate waveguide devices.

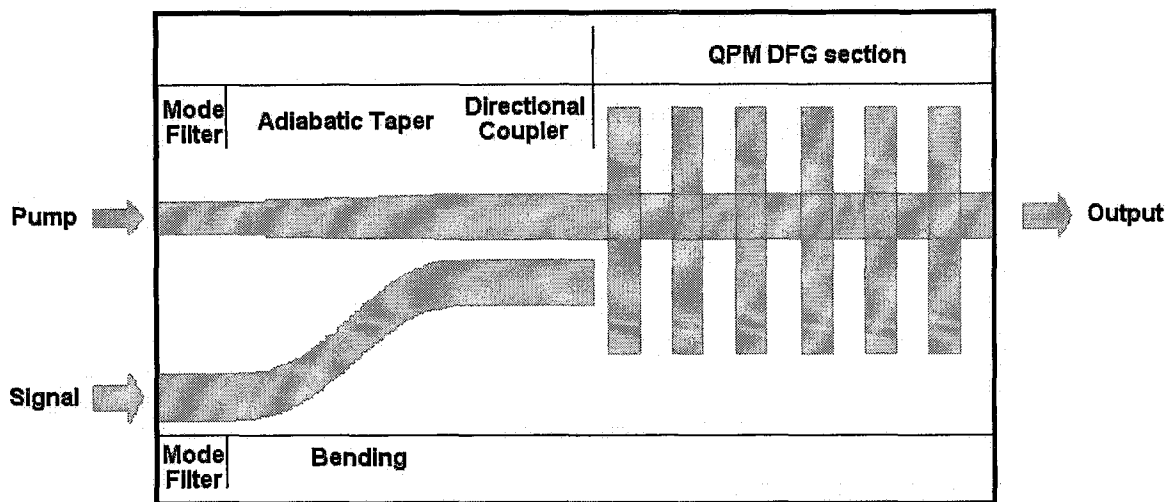


Fig.4.2 schematic diagram of DFG wavelength conversion device including integrated coupling structure

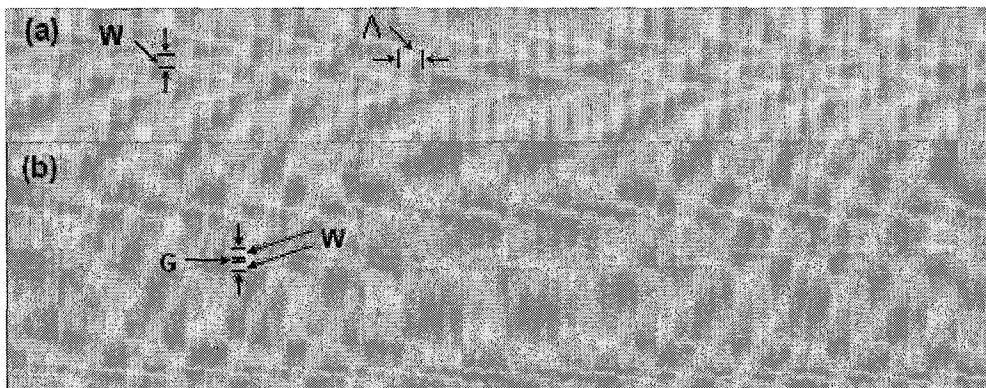


Fig.4.3 Micrograph of integrated coupling structure on PPLN waveguide device: a) part of adiabatic taper and bending, b) part of directional coupler. The domain walls are vertical straight lines and light propagates horizontally along waveguides. W is the wavelength width $\sim 8 \mu m$, Λ is the QPM period $\sim 19.5 \mu m$ and G is the gap between two adjacent waveguide $\sim 2.5 \mu m$.

The integrated coupler on the LiNbO₃ devices replaces a normal optical fiber and WDM coupler. In comparison with the WDM fiber coupler, the integrated WDM coupler on lithium niobate can facilitate the coupling of the pump wave and signal wave to the waveguide independently, and has the possibility of integrating the waveguide devices with other functional devices on a single chip to construct the optical integrated circuit. In optical integrated circuit, precise position and assembly are not necessary, and stable alignment is maintained.

4.3 Mode-filters and input tapers

The input waveguide region with a few mm long is often called “mode filter”. It is designed to guide the lowest order mode at input wavelength, while keeping low-loss coupling from a commercial single mode fiber (SMF).

The mode field diameter ($1/e^2$) for a commercial 780 nm SMF is around $5.0 \mu\text{m}$. The input mode size of the mode filter can be controlled by waveguide width. To get the optimal width of fiber mode matching, we fabricate straight waveguide with mask width of $2\mu\text{m}$, $3\mu\text{m}$, $4.5\mu\text{m}$, $5\mu\text{m}$, $8\mu\text{m}$. The experimental result shows that only waveguide with mask width of $2 \mu\text{m}$ is single-mode waveguide for 780nm. Fig.4.4 shows a measured mode profiles at wavelength of 780nm for waveguide mask width of $2 \mu\text{m}$, with measured mode size of $6.5 \mu\text{m} \times 4.8 \mu\text{m}$ ($1/e^2$) or (FWHM) $3.7 \mu\text{m} \times 2.7 \mu\text{m}$ (width \times depth).

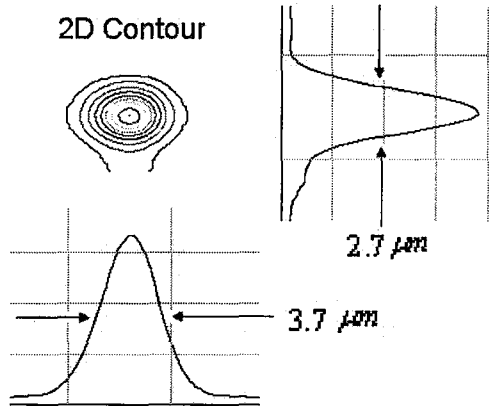


Fig.4.4 measured mode profile at $\lambda = 780\text{nm}$ for waveguide mask width of $2 \mu\text{m}$.

A $2 \mu\text{m}$ -wide waveguide has a single mode much better suited in size and shape for fiber-waveguide coupling. A mode mismatch loss between $2 \mu\text{m}$ -width waveguide and single mode fiber for 780nm is calculated by BPM-CAD software under 0.2 dB. The calculation is based on the power overlap integral (POI) of the waveguide and fiber, which is defined as

$$POI = \frac{\left| \int_{\text{mesh}} E_1(x, y) \cdot E_2^*(x, y) dx dy \right|^2}{\int_{\text{mesh}} |E_1(x, y)|^2 dx dy \cdot \int_{\text{mesh}} |E_2(x, y)|^2 dx dy} \quad (4.1)$$

The mode field diameter ($1/e^2$) for a standard 1550 nm SMF is around $9.0 \mu\text{m}$. The single-mode waveguide for 1550nm is fabricated with waveguide mask width of $8 \mu\text{m}$ by experience in our group. The measured mode profile is shown in Fig.4.5, with a mode size of $9.82 \mu\text{m} \times 6.53 \mu\text{m}$ ($1/e^2$) or $5.78 \mu\text{m} \times 3.84 \mu\text{m}$ (FWHM) (width \times depth) at wavelength of 1550 nm. Mode-mismatch losses are calculated as 0.2 dB.

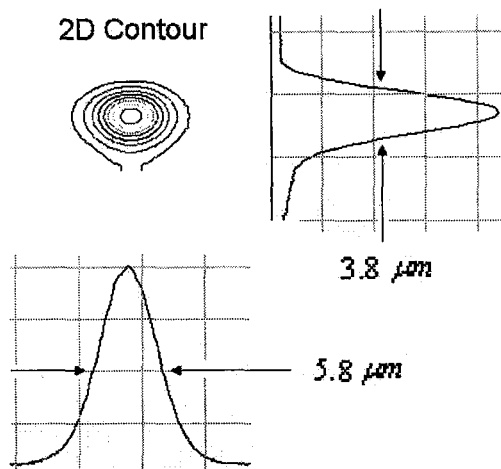


Fig.4.5 Measured mode profiles at $\lambda = 1550\text{nm}$ in the wavelength conversion section with waveguide mask width of $8\ \mu\text{m}$

The waveguide mode size is not a linear function of mask width due to the nonlinear diffusion in the fabrication process. In narrow waveguide region, the mode width decreases as the waveguide width increases due to the improved confinement. In the wide waveguide region, the mode width increases as the waveguide width increases because the waveguide geometry dominates the mode size. [3] In the transition region, the waveguide mode size gets its minimum to improve the conversion efficiency, and is less sensitive to width variation to increase the fabrication tolerance. According to the results in our group, the width of the wave mixing region is chosen as $8\ \mu\text{m}$. Fig. 4.5 shows a measured mode profiles at wavelength of 780nm in the multi-mode section for width of $8\ \mu\text{m}$, with measured mode size of $5.54\ \mu\text{m} \times 3.67\ \mu\text{m}$ ($1/e^2$) or $3.2\ \mu\text{m} \times 2.1\ \mu\text{m}$ (FWHM) (width \times depth).

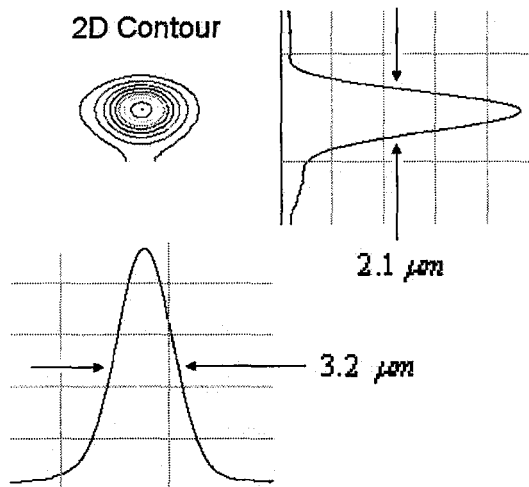


Fig.4.6 Measured mode profiles at $\lambda = 780\text{nm}$ in the multi-mode section with waveguide mask width of $8\ \mu\text{m}$

It is shown that an adiabatic taper is required to launch the pump from single mode of the mode filter into the fundamental mode of the wave mixing regions. [7] Both periodically segmented taper and continuous taper have been reported in Ref.[3]. The configurations are shown in Fig. 4.7.

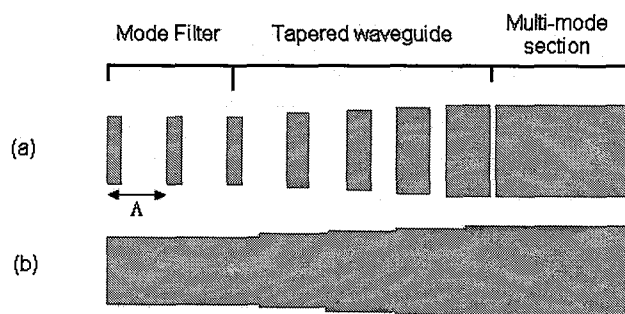


Fig.4.7 schematic plot of two different adiabatic taper in waveguide: a) segmented structure and b) continuous lateral taper

While the segmented taper waveguide can taper both lateral and vertical dimension of the waveguide, it introduces some excess losses due to a highly non-continuous structure and demands higher fabrication techniques. [3] For simplicity, continuous lateral taper is fabricated by standard photolithographic techniques in this work. As shown in Fig. 4.4, the narrower waveguide channel on the mask at the input is connecting the wave mixing region by an adiabatic taper. By gradually varying the width of the waveguide mask opening, the cross-section of the guided beam is slowly contracted with proper mode conversion. The taper angle in the transition region is sufficiently small to prevent coupling of power from the fundamental mode into the higher order taper modes. The adiabatic taper acts as a mode size converter.

Regarding on the waveguide edge curvature, there are several tapers with a few mm long for different taper profiles, Fig.4.8 shows three taper profiles of linear, S-sin and exponential taper.

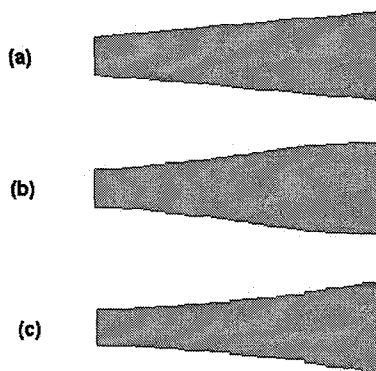


Fig. 4.8 Taper types of a) linear, b) S-sin, C) exponential

BPM-CAD software is used to find an optimum taper-profile which requires a minimum taper length while keep effective power transfer. The simulation shows that for the same taper length, taper losses of linear profile and S-sin profile are comparative, while exponential profile has much less taper loss and is recommended in the design. The experimental results agree with the simulation.

4.4 Directional coupler

Directional coupler is probably the most common WDM component to combine pump and signal light with low insertion loss. It is composed of two parallel waveguides that are close to each other with a gap only on the order of several wavelengths. In the directional coupler, modes of each waveguide overlap and optical power are transferred from one waveguide to another as they propagate over a characteristic distance.

The fundamental concept of directional coupler is as follows. As mentioned in Chapter 2, various guided modes exist in a lossless waveguide which is uniform along the propagation direction. An orthogonal relationship holds among these normal modes which are defined by the waveguide structure and its boundary conditions. Thus, each mode propagates without mutual coupling and carries power independently.

However, in a perturbed waveguide systems, normal modes are not independent and coupled mutually. Consider a simple case of two waveguides I and II, as shown in Fig.4.9. When they are separate enough from each other, two normal modes a and b propagate independently on each waveguide with field ψ_a and ψ_b , and propagation constants β_a and β_b ($\beta_a < \beta_b$), respectively. When the separation is reduced, the original normal modes ψ_a and ψ_b no longer exist, and two new normal modes ψ_o and ψ_e propagate along a coupled waveguide system consisting of waveguide I and II, as shown in Fig.4.9 (b), with propagation constants β_o and β_e ($\beta_o < \beta_a, \beta_e > \beta_b$). ψ_o and ψ_e correspond to odd mode and even mode, respectively.

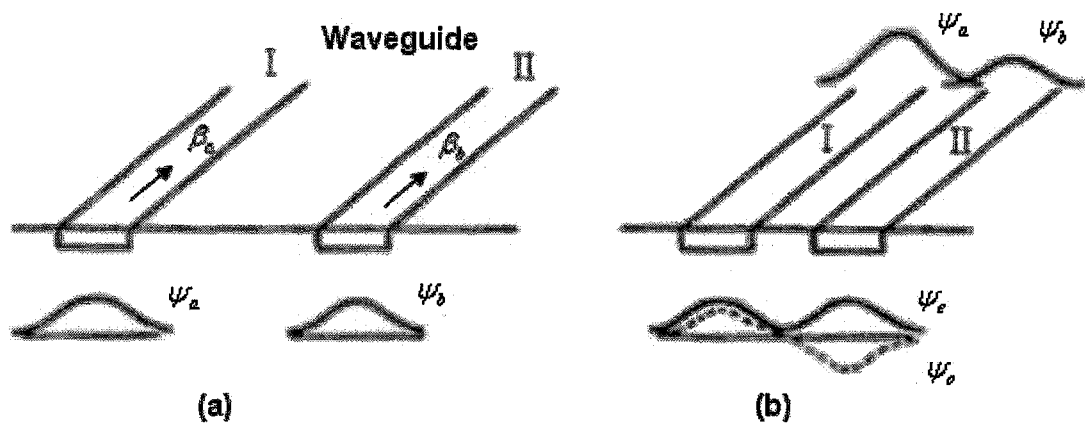


Fig.4.9 Normal modes in two waveguide in the absence and presence of coupling[14]

The power transfer mechanism can be well understood by interference between the normal even and odd modes in the coupling region. Consider a typical directional waveguide coupler, as shown in Fig.4.10. The coupling takes place in the $0 < z < L$ region.

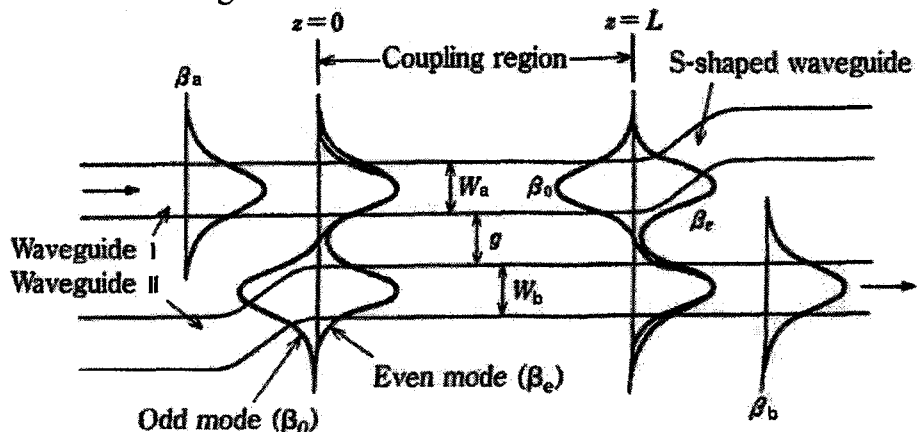


Fig.4.10 Operating principle of waveguide directional coupler[14]

The guided mode incident from waveguide I excites the even and odd modes of the waveguide coupler in phase with the same amplitude at $z=0$. As the propagation constants β_o and β_e are slightly different from each other, the two modes yield a beat. The phase shift between the even and odd modes becomes π when the propagation distance L is

$$L_c = \frac{\pi}{\beta_e - \beta_o} \quad (4.2)$$

where L_c is defined as the coupling length. Hence, at output end of the coupling region $z=L_c$, the resultant electric field distribution of the even and odd modes

coincides with the electric field distribution of the guided mode in waveguides II. When looking at wave behaviour along waveguides I and II, wave power appears to transfer back and forth periodically between I and II (that is, between ψ_a and ψ_b). The power transfer rate is as

$$P(z) = P_0 \sin^2\left(\frac{\pi L}{2L_c}\right) \quad (4.3)$$

The coupling effects appear stronger when β_a and β_b are approximately equal. If the two waveguides are identical, 100 percent power can be transferred. [14] By adjusting the length of the coupling region, different power transferring ratio can be achieved. A directional waveguide coupler with 50% power transferring ratio is used as beam splitter.

The coupling mechanism can also be understood by coupled mode propagation along two coupled waveguides. Optical waves ψ_a and ψ_b propagating along the coupled waveguide I and II are expressed as

$$\psi_a(x, y, z, t) = A(z)e^{-j\beta_a z} f_a(x, y)e^{j\omega t} \quad (4.4 a)$$

$$\psi_b(x, y, z, t) = B(z)e^{-j\beta_b z} f_b(x, y)e^{j\omega t} \quad (4.4 b)$$

Where f_a and f_b are field distribution functions that are normalized by power flow over a cross section. If coupling between I and II is reduced to zero, ψ_a and ψ_b are reduced to two independent original normal modes, and $A(z)$ and $B(z)$ are reduced to constants. When coupling is present, $A(z)$ and $B(z)$ are no longer independent. The coupled mode equations are as follows:

$$\frac{dA(z)}{dz} = -j\kappa_{ab}B(z)e^{-j(\beta_b - \beta_a)z} \quad (4.5 a)$$

$$\frac{dB(z)}{dz} = -j\kappa_{ba}A(z)e^{+j(\beta_b - \beta_a)z} \quad (4.5 b)$$

Where κ_{ab} and κ_{ba} are coupling coefficients between two modes. It is spatial overlapping of normal modes over dielectric constant increments $\Delta\epsilon$ in waveguide II, as shown in Fig.4.11, and is calculated by the following integral:

$$\kappa_{ab} = c \int_{II} f_a^* \Delta\epsilon f_b dx dy \quad (4.6)$$

Where the integration range is the cross section of waveguide II, and c is a constant related to the normalization of ψ_a and ψ_b .

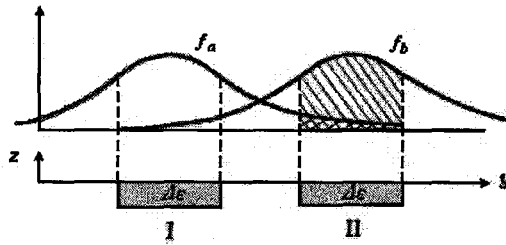


Fig.4.11 explanation of integration for calculation of coupling coefficients.[14]

The term $e^{\pm j(\beta_b - \beta_a)z}$ on the right-hand side corresponds to the phase-constant mismatching of the modes. When $\kappa_{ab} = \kappa_{ba} = 0$, $A(z)$ and $B(z)$ reduced to $A(z) = A_0$ (constant) and $B(z) = B_0$ (constant).

The coupling length L_c can be calculated based on the coupled-mode equations (4.5), and is a function of the mode overlap between two adjacent waveguides.

Taking advantage of the available numerical simulation tools of BPM-CAD, the power transferring was simulated and shown in Fig.4.12, and the coupling lengths of annealed proton-exchanged directional couplers are calculated and shown in Fig.4.13.

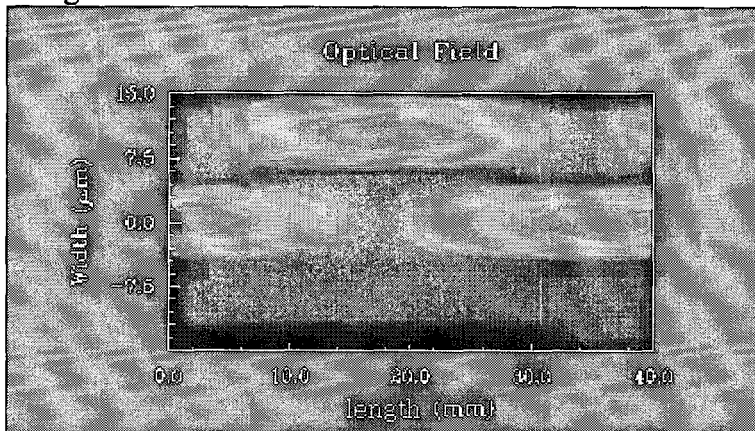


Fig.4.12 simulation of power transfer for directional coupler

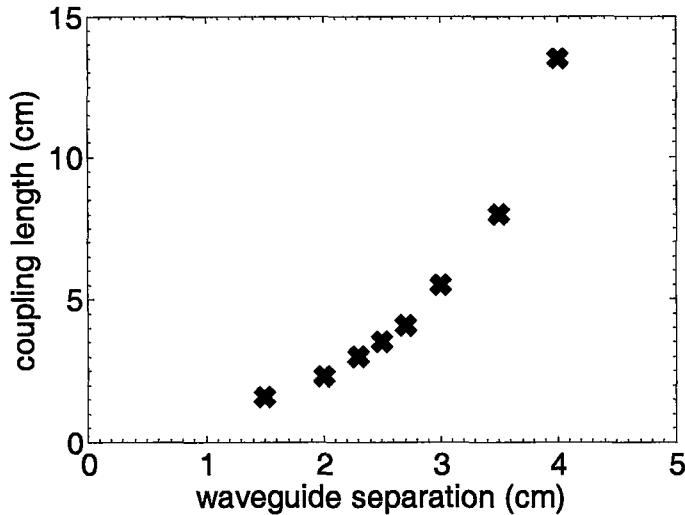


Fig.4.13 simulated coupling lengths vs. waveguide separation for waveguide width of $9 \mu\text{m}$.

While trends carry over from simulation to experiment, small differences between the simulated and actual index profiles will result in difference of mode overlap between two adjacent waveguide, thus in significantly different coupling lengths. The index profile is sensitive to waveguide width variation even with the same waveguide center-to-center separation. In practice, the waveguide width is sensitive to the fabrication processes, such as photolithography, etching, proton-exchange, etc.

Due to this uncertainty, we empirically determine the length of a directional coupler for a chosen spacing between the two arms. A large number of directional couplers with the same edge-to-edge separation are fabricated with different waveguide widths and different interaction length. The waveguide separation was set as $2.5 \mu\text{m}$. The waveguide width varied as $8 \mu\text{m}$, $8.5 \mu\text{m}$ and $9 \mu\text{m}$. Coupling lengths in the range of $1.6 \sim 5\text{mm}$ was chose as a good compromise between expected performance and space requirements

The coupling ratio of the directional coupler, or called extinction ratio, is a measurement of coupler performance. When the power is incident into the waveguide A, without the loss of generality, the coupling ratio after a distance equal to the coupling length is defined as P_b / P_a where P_a and P_b are the guided powers in waveguide A and B respectively. The coupling ratio is wavelength dependent.

The directional coupler in our work is designed to get the maximum signal coupling from signal path to conversion section and meanwhile minimize the pump coupling out of conversion section. Thus the optical fields at pump and signal are combined into the same waveguides to achieve the function of wavelength multiplexing. Fig.4.14 shows the expected sinusoidal dependence of

the coupling ratio at wavelength of 1550nm on the interaction length. Maximal coupling ratio at $\lambda=1550$ nm is 25.4dB for coupler with length of 1.7mm and waveguide width of $8\ \mu\text{m}$. Compared to simulated coupling length in Fig.4.13, our current waveguide model may have >20% error in such a simulation.

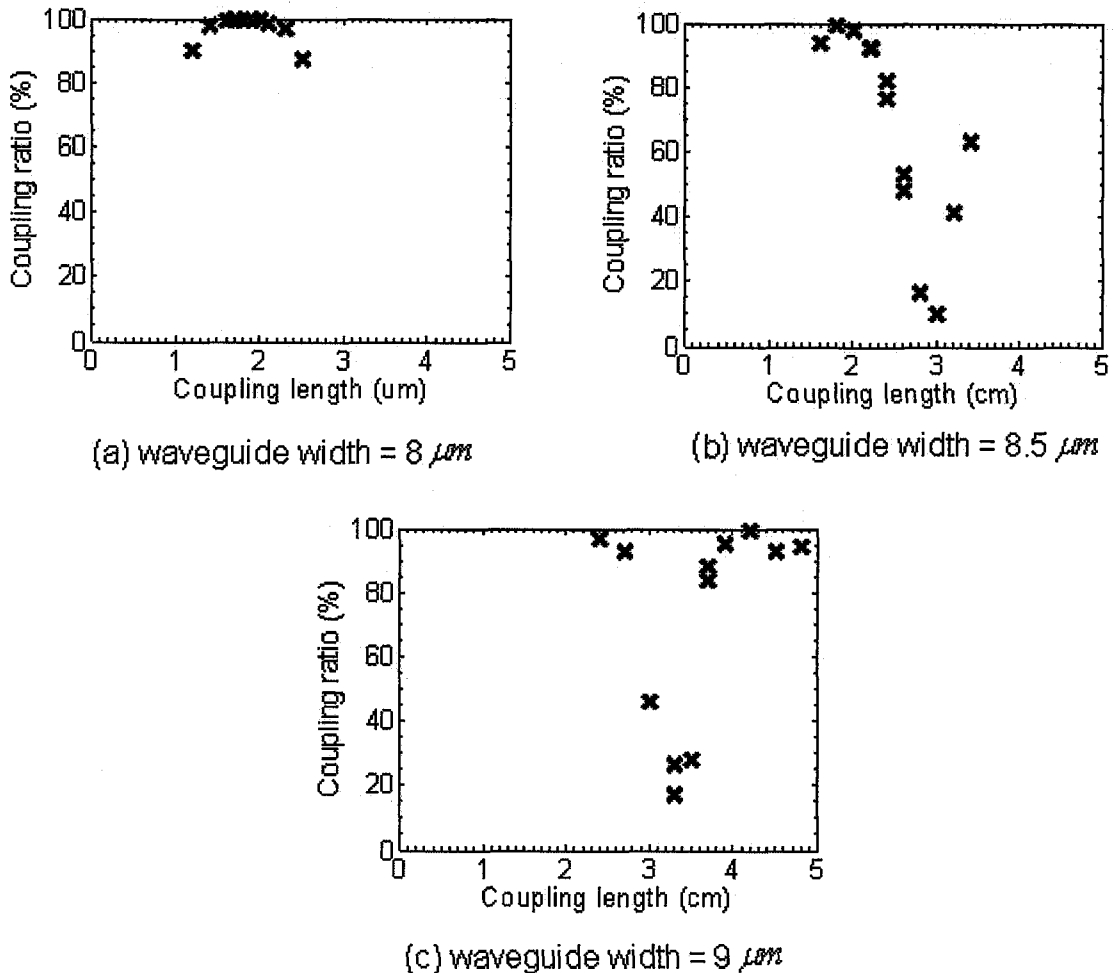


Fig.4.14 Measured coupling ratio of signal with $\lambda=1550$ nm into conversion section as a function of coupler length (cm) for coupler waveguide width of a) $8\ \mu\text{m}$, b) $8.5\ \mu\text{m}$, c) $9\ \mu\text{m}$ while keeping waveguide separation of $2.5\ \mu\text{m}$.

4.5 Small radius bending

When optical fibers are connected into the input end of a directional waveguide coupler, the separation between two input waveguides must be larger than the clad diameter of the fiber, which is typically $150\ \mu\text{m}$. A typical separation of directional coupler is 2- or $3\ \mu\text{m}$, which is much smaller than the input waveguide separation. So optical path bending is necessary near the input end to change the optical path direction.

In this work, the input end of the device is made with a separation of $500\ \mu\text{m}$ to accommodate the fiber array, which is made of V-groove and is shown in Fig.4.15.

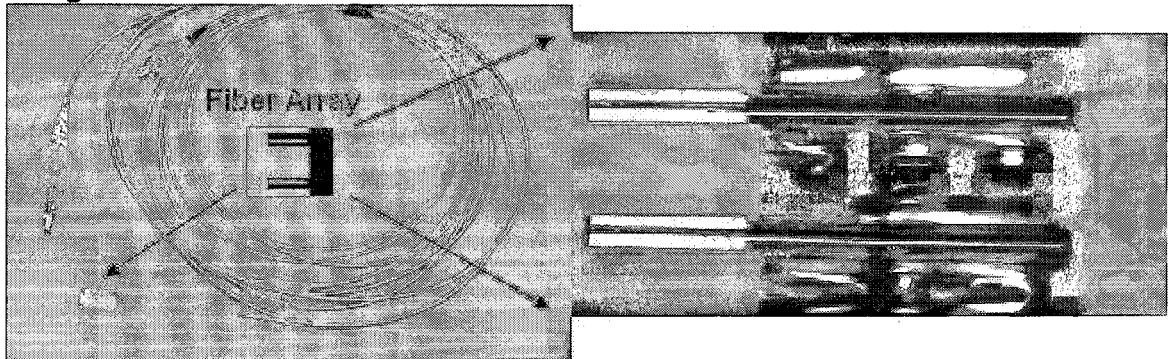


Fig.4.15 fiber array made of V-groove

Fig.4.16 Show the required connection of two straight waveguides with offsets of l as the longitudinal separation in the x direction and as the lateral offset in the y direction. This simple connection method is to use corner-bent waveguide, as shown in Fig.4.16. However, the guided waves suffer remarkable scattering loss at two corners. This loss cannot be totally suppressed unless the corner angle is much smaller than 1 degree. Consequently, l is substantially more than 100 times as long as h .

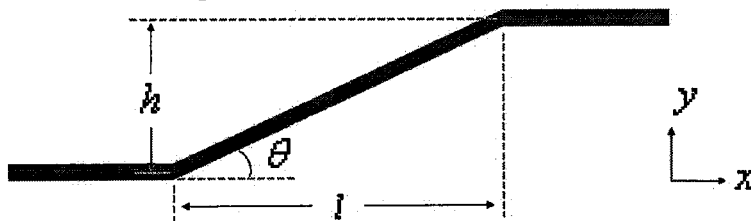


Fig.4.16 Corner-bent waveguide for path bending

For a certain value of h , l is as short as possible with minimal connection loss. Thus S-shaped waveguides with smoothly curved waveguide is considered. There are three different schemes of S-shape shown in Fig.4.17: a) circular bending, b) S-Sin bending and c) S-Cos bending.

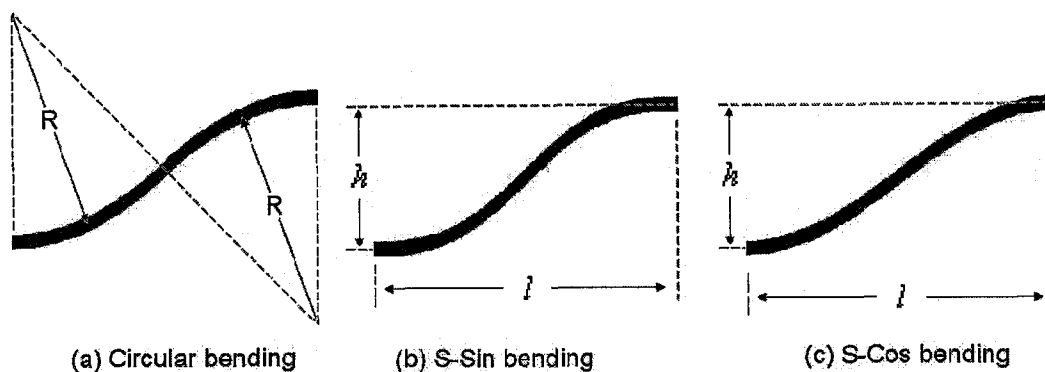


Fig.4.17 S-Shaped waveguides for path bending

Circular bending waveguide is formed by connecting two $\pi/4$ -arc waveguides with a uniform radius curvature. This circular waveguide, however, has a significant disadvantage in that remarkable mode conversion loss occurs at the junction between two arc waveguide due to an optical field mismatch. To avoid this problem, the radius curvature of the S-shaped waveguide must be changed gradually along the propagation direction. Thus, sin type S-bends waveguide and cosine type S-bends waveguide was designed using the following shape functions:

S-Sin wave function:

$$y = \frac{h}{l}x - \frac{h}{2\pi} \sin \frac{2\pi}{l}x \quad (4.7)$$

S-Cosine wave function:

$$y = \frac{h}{2} \left(1 - \cos \frac{\pi}{l}x\right) \quad (4.8)$$

Where x , y are the length and height dimensions respectively, h is the height and l is the length. This shape function is the center line of the waveguides defined on the mask for proton exchange.

A small bend radius is desired to enhance device integration. As the curvature radius R becomes smaller, an optical-path direction is changed at a shorter propagation distance. However, it is limited by rapidly increasing radiation losses and decreasing mode confinement with decreasing bend radius. Propagation loss in bends includes radiation loss coming from mode coupling into radiation modes, transition loss coming from the mode mismatch at the junction of curvature discontinuity, and scattering loss coming from the roughness or defects in the waveguide structure.

BPM CAD program was used to generate Fig.4.18, which gives visual predictions of the behaviour of a light wave propagating through a circular waveguide, an S-cos bend waveguide and an S-sin bend waveguide with the same radius. It is shown that if the minimum bend radii are the same, the radiation loss of circular bends is larger than that of s-bends. The S-cos bend waveguide gives the lowest bending loss.

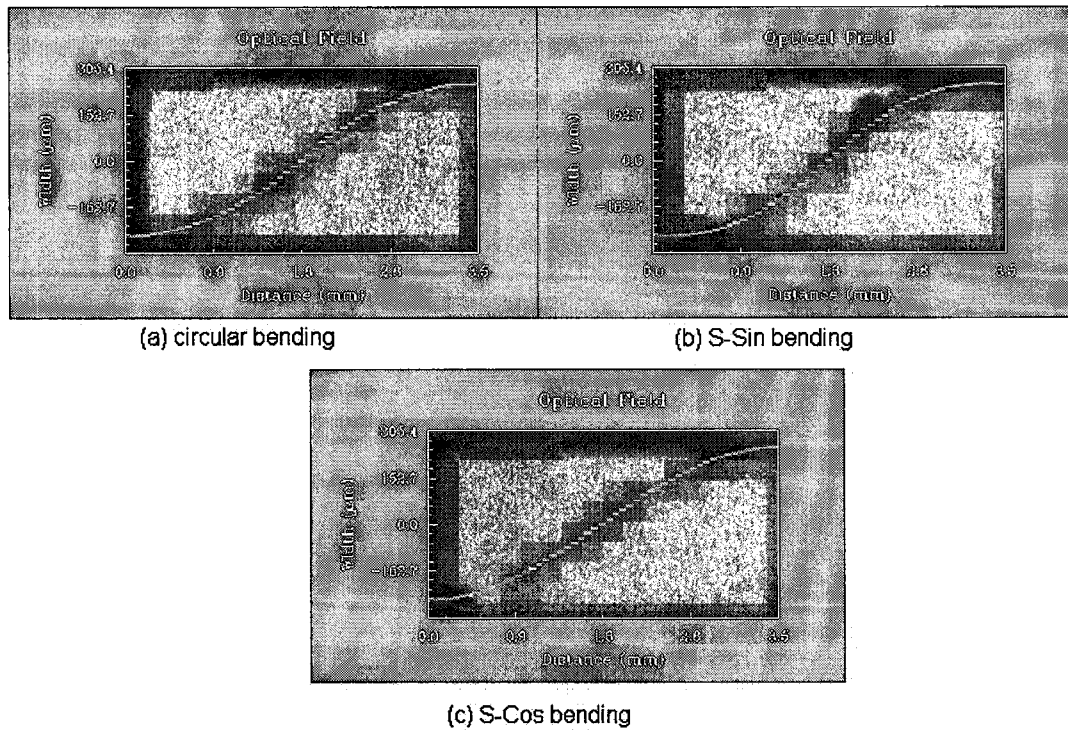


Fig.4.18 Simulation of electric field distribution in a) circular bending, b) S-Sin bending and c) S-Cos bending waveguides with $l=3.5$ cm.

BPM-CAD was used to calculate the bending loss of the bent waveguide with different bend radius and different index profile. The calculated results suggest that deeper proton-exchange can reduce the minimum bend radius. Increasing the proton-exchange depth, the effective refractive index of the waveguide modes increases and the mode size in the dimension of the waveguide width shrinks, thereby the minimum bend radius is much smaller from the following equation:

$$R_{\min} \sim \frac{\rho n_{\max}}{n_{\text{eff}} - n_0} \quad (4.9)$$

However, increasing the proton-exchange depth introduce higher propagation loss in straight waveguides. This higher propagation loss is mainly scattering loss caused by the larger quantity of defects in the waveguides with a higher proton dose. The proton exchange depth in the fabrication process is optimized for a balance between the small bend loss and the small propagation loss in straight waveguides.

To explore each bend design and find the optimal condition, the bends are fabricated with different designs and lengths. The bend losses of each bend design is measured and shown in Fig.4.19. The figure shows that bend loss increases exponentially when the length decreases. The smallest bending length without

significant bend losses is around 6mm for S-cos bends ($h=500\mu\text{m}$ and $l=6\text{mm}$) with bend radius of 14mm.

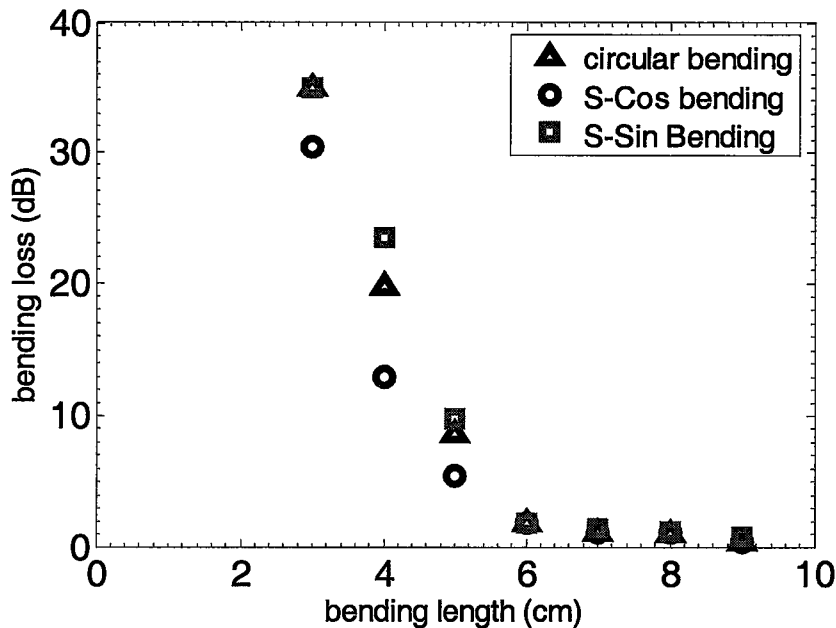


Fig.4.19 Bending loss vs. bending length for circular, S-cos and S-sin bends

4.6 Modeling of the device structure

This section provides some details on modeling lithium niobate waveguide device structure, which is capable of de-multiplexing two wavelengths into DFG region. Based on beam propagation method and the coupled mode theory, the mode-coupling components described in Chapter 3 and nonlinear frequency-mixing sections were simulated separately and predict the experiment results.

Modeling of integrated coupling structure

Beam propagation method (BPM) was used to develop and optimize the design of integrated coupling structure. It is a step by step method of simulating the light propagation through any waveguide medium. It is a numerical simulation of the electric field in a waveguide, not an approximate solution of the exact wave equation. BPM is very useful in determine the mode profile in an unusual waveguide and the dynamic behaviour of a mode as the index profile changes at cross section of waveguide along propagation. Beam propagation theory is based on the assumption of a plane-polarized beam, which in turn entails the assumption of paraxiality, although in certain cases non-paraxiality may be taken into account approximately.

The beam propagation method is available as computer-aided design (CAD) software tools. A commercial waveguide optics modeling software program of BPM CAD (Optiwave Corporation) was utilized to develop the waveguide structure design.

The user defined refractive index profile of diffused waveguide is used in BPM CAD to optimize the design. The refractive index of the material is calculated from temperature-dependent Sellmeier equation in 3.4. The refractive index distribution of waveguide is generated with the model in 3.3. The design parameters include operating wavelength, the proton-exchange time, the annealing time, waveguide width, etc. Zero propagation loss was assumed for the straight guides.

The graphical device layout of integrated coupling structure created by BPM-CAD software is shown in Fig.4.20. The waveguide width is $8\mu\text{m}$ and gap between waveguide is $2.5\mu\text{m}$. The directional coupler length is 1.7mm .

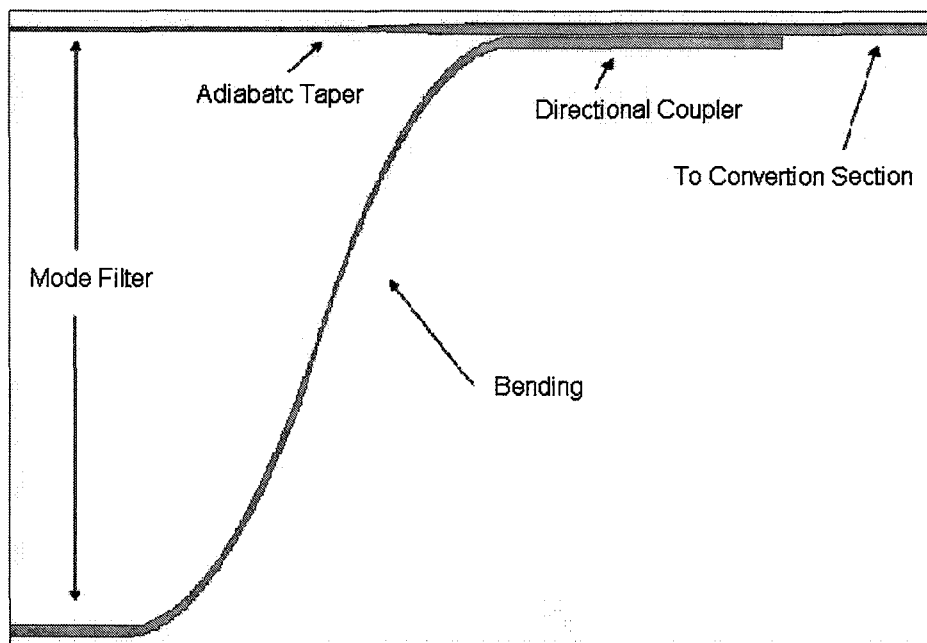


Fig.4.20 BPM layout for integrated structure

The software calculates the amplitudes of the electric fields as they propagate through the medium. The simulation result of signal input is shown in Fig. 4.21, where the light signal was diverted by bending waveguide, and demultiplexed into the preferred conversion waveguide.

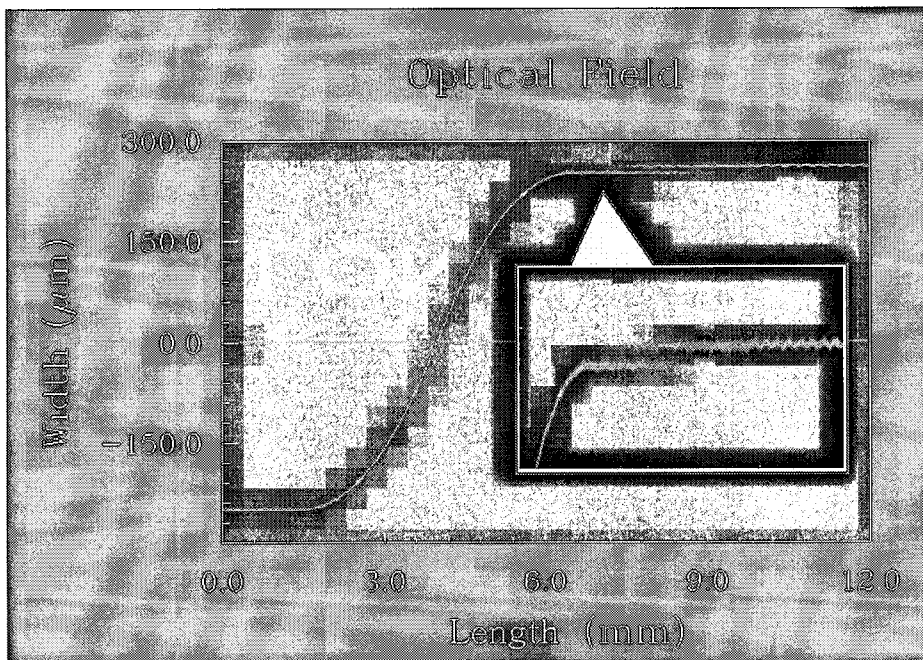


Fig.4.21 optical field distribution of the signal light propagation

The simulation result of pump input is shown in Fig.4.22, where the pump convert its mode size when propagating through the adiabatic taper, and keep most power in the preferred conversion waveguide.

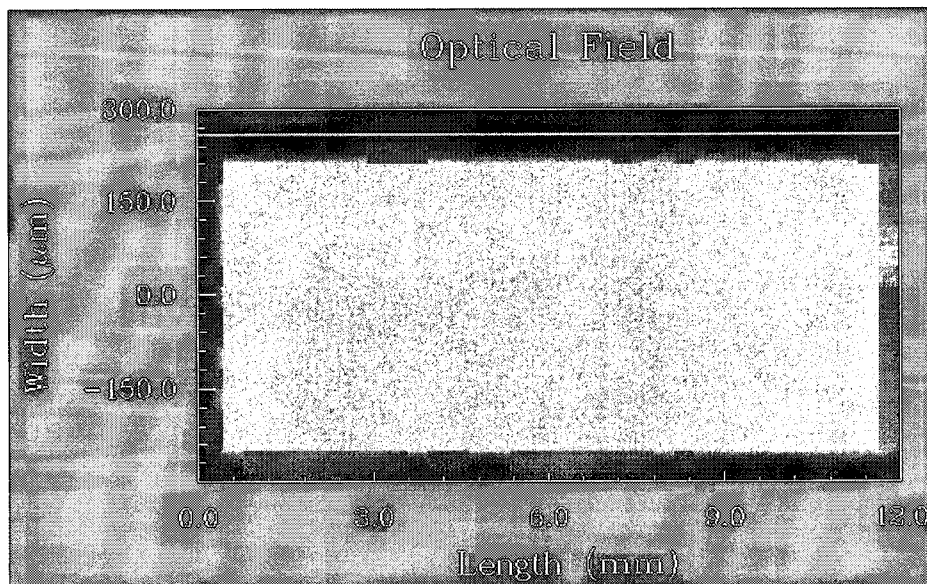


Fig.4.22 optical field distribution of the pump light propagation

The basic theory on each component of the integrated coupling structure is discussed in 4.3, 4.4 and 4.5, and each component is simulated and analysed separately to optimize parameters.

Simulation of DFG section:

The integrated coupling structure is passive component, and can be modeled simply as insertion losses. The DFG wavelength conversion section is active components, and modeling is slightly more complicated.

The simulation of DFG conversion process is based on the coupled mode equation, which can be found in Chapter 2 and rewrite here:

$$\frac{dA_p}{dz} = -j\omega_p \kappa A_s(z) A_{out}(z) \exp(j\Delta kz) - \frac{\alpha_p}{2} A_p \quad (2.20.a)$$

$$\frac{dA_s}{dz} = -j\omega_s \kappa^* A_{out}^*(z) A_p(z) \exp(-j\Delta kz) - \frac{\alpha_s}{2} A_s \quad (2.20.b)$$

$$\frac{dA_{out}}{dz} = -j\omega_{out} \kappa^* A_s^*(z) A_p(z) \exp(-j\Delta kz) - \frac{\alpha_{out}}{2} A_{out} \quad (2.20.c)$$

where the phase velocity mismatch due to material dispersion is:

$$\Delta k' = k_p - k_s - k_{out} - \frac{2\pi}{\Lambda} \quad (2.40)$$

and $k_i = 2\pi n_i / \lambda_i$ is the propagation constant at the corresponding frequency, $i = p, s$, or out , λ_i is wavelength in vacuum, n_i is refractive index at that wavelength. Λ is the QPM period. The constant κ is defined as

$$\kappa = \varepsilon_o d_{eff} \sqrt{\frac{1}{2n_e(\lambda_p)n_e(\lambda_s)n_e(\lambda_{out})A_{eff}} \left(\frac{\mu_0}{\varepsilon_0} \right)^{3/2}} \quad (2.22)$$

where d_{eff} is the effective nonlinear coefficient,

$$d_{eff} = \frac{2}{\pi} d_0 \quad (2.41)$$

and the effective area A_{eff} is defined as

$$A_{eff} = 1/v^2,$$

where v is overlap integral and defined as

$$v = \int_{-\infty}^{\infty} \int_{-\infty}^{\infty} d(x, y) E_s(x, y) E_{out}(x, y) E_p^*(x, y) dx dy \quad (2.23)$$

α_i ($i = p, s$, or out) is the propagation loss at corresponding frequency. n_c, n_p and n_s are the refractive indices for the converted, the input pump and the input signal light, respectively. ε_0 is the permittivity of free space.

In the simulations, the conversion length was set to 4 cm. The grating period was set to $19.5 \mu\text{m}$. The nonlinear coefficient of Lithium niobate d_0 is set as 27 nm/V . A_{eff} is the cross sectional area of the waveguide, which is 53 um^2 .

The refractive indices at different wavelengths were determined from temperature-dependent Sellmeier equation in 3.4. And the simulation result is shown together with the experimental result in Chapter 5.

Chapter 5

Wavelength converter with integrated coupling structure

In this chapter, I will show the performance of DFG wavelength converter based on periodic poled MgO:LN with integrated coupling structure described in Chapter 4 and fabricated with the fabrication techniques in Chapter 3.

5.1 Basic device information

To demonstrate the performance of wavelength converter, we fabricated the waveguides by annealed proton-exchange in z-cut 0.4-mm-thick periodically poled 5mol% MgO doped lithium niobate substrate. The 5.0 cm long device includes an integrated waveguide structure for efficient mode coupling, and a 4.0 cm long wavelength conversion section, as shown in Fig.4.2. In the conversion section, periodically domain inverted structure has a duty cycle of nearly 50% and a period of about 19.5 μm , and the waveguide is along the x axis and has a width of 8 μm . The proton exchange and thermal annealing were carried out at 200 $^{\circ}\text{C}$ for 2h 20min and 350 $^{\circ}\text{C}$ for ~6 h, respectively.

5.2 Loss measurement

In characterizing the performance of the device, the total fiber-to-fiber insertion loss is of high concern. The total insertion loss include propagation loss, which is one of the major limiting factors to maintain high transmission efficiency, and the end fire coupling losses, which include the following three main parts.

First of all, due to the difference in refractive index of the fiber and waveguide core materials, there are reflection losses at the facet of the input fiber and the waveguide input. Also, due to the air gap between the fiber and the waveguide and the values of both indices are larger than 2 in all transparency regions, there may be some diffraction and Fabry-Perot (multiple reflections) effects which can cause a slight oscillation of the insertion loss. Using anti-reflection coating on the fiber and waveguide facets or UV epoxy between the two facets would assist in reducing the insertion loss due to the reflection.

Second is a mode size and shape mismatch loss, minimum of which occurs when the field incident upon the waveguide after the diffraction has the maximum overlap integral with the electric field of the waveguide. Standard single mode fibers have circular shape, while waveguide typical has elliptical shape. To get optimal mode matching, waveguides with different mask width are fabricated and tested. More details can be found in 4.3.

Finally, fiber-waveguide couplings are very sensitive to angular misalignment, so care should be taken to ensure that the fiber and the waveguide are as parallel as possible. Also, transverse misalignment has more effect on the coupling loss than longitudinal misalignment. Fig.5.1 shows the transverse, longitudinal and angular misalignment between a fiber and a waveguide. Proper alignments of the fiber to the waveguide facets are critical and it is important to minimize optical loss at these connections as effectively as possible.

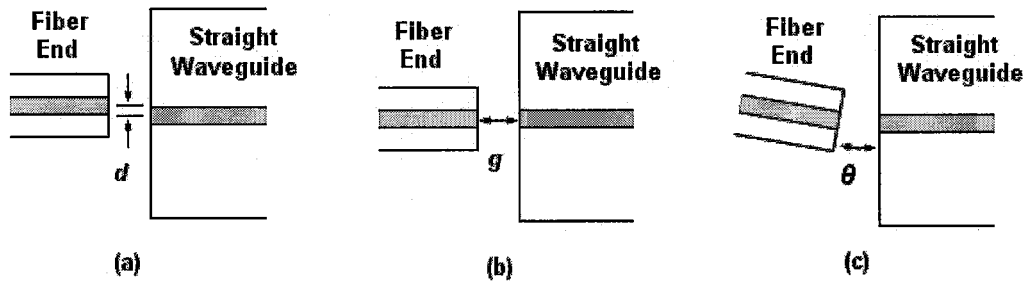


Fig. 5.1 schemes of misalignments between fiber and waveguide. a) transverse misalignment, given by the offset d between the centers of the fiber and the waveguide. b) longitudinal misalignment, given by the gap g between the fiber and the waveguide, c) angular misalignment, given by the angle θ of facets of the fiber and waveguide end.

The total insertion loss was measured to be less than 4.5 dB at 1550 nm and less than 8.5 dB at 780 nm for straight waveguide with 8 μm width on the devices. The end fire coupling loss was estimated to be around 0.7dB at 1550 nm and 1dB at 780 nm. The estimated propagation loss is around 0.6dB/cm at 1550 nm and 1.3dB/cm at 780 nm.

5.3 SHG measurement

In telecommunications band, SHG is a very useful diagnostic to characterize devices based on near-degenerate three wave mixing interactions such as SFG and DFG, which are more complicated processes. The reason is that the value of normalized DFG efficiency for nearly degenerated case is approximately equal to that of normalized SHG efficiency. Therefore, preliminary characterization of the DFG device was carried out by simple SHG experiments.

A fundamental wave from a broadband source was coupled to the lowest order mode of the signal waveguide input of the device by end-fire coupling. The optical spectra of the fundamental wave and second harmonic wave were measured with an optical spectrum analyzer (OSA, Agilent 81642A) with a resolution of 0.1nm. The measured and theoretical CW SHG tuning curve for this device is shown in Fig. 5.2. The measured full-width at half-maximum (FWHM) of the tuning curve is $\sim 0.33\text{nm}$. The peak efficiency of the calculated curve is chosen such that the areas under the measured and calculated curves are equal.

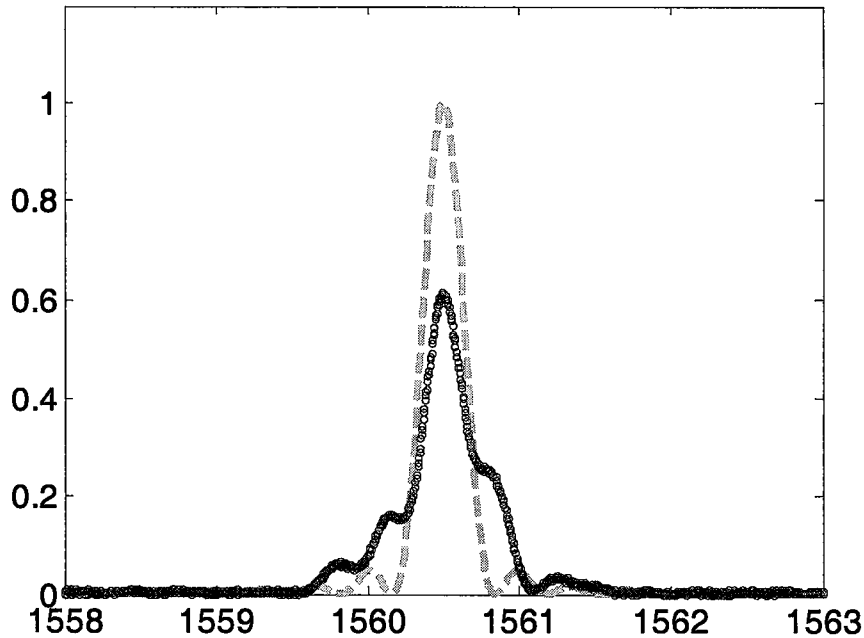


Fig.5.2 measured CW SHG tuning curve (circle marks) and theoretical sinc² tuning curve (dashed line). Distortion is observed between measurement and calculation.

The deviation of the measurement from the calculation reveals variations of residual phase mismatch along the length of the device, which arises from slight imperfections on the uniformity of periodically domain-inverted grating and waveguide in the fabrication process. While standard QPM devices tend to have tight fabrication tolerances set by the phase-matching bandwidth, integrated optics structures reduce these tolerances much further. Increasingly complicated device geometries require fabrication parameters with higher precision in improving waveguide uniformity and maintaining QPM uniformity over a long interaction length. Whether these variations come from the proton-exchange, the annealing, the lithography, or other sources is unknown. However, several possible factors are worth investigating. The lithography process can introduce some waveguide non-uniformity, due to uneven illumination and contact between the mask and wafer. The transparency of lithium niobate also leads to unwanted reflections within the wafer during exposure. The periodic poling process introduces slight index variations at domain boundaries, and translates into waveguide width variation.

Typical spectrum of fundamental wave and second harmonic wave measured at the device output is shown as Fig. 5.3. The exact QPM wavelength of fundamental wave was measured to be 1560.9nm in the continuous wave (CW) regime at room temperature. The standard peak efficiency for this device with a

grating length of 4cm is 445 %/W (\approx DFG efficiency), defined as

$$\eta_s = \frac{P_{SHG}^{out}}{(P_f^{out})^2} \times 100\%. \text{ So the normalized efficiency is } 27.8\% / W \cdot cm^2, \text{ defined as}$$

$$\eta_{nor} = \frac{P_{SHG}^{out}}{(P_f^{out})^2 L^2} \times 100\%. \text{ The black box peak efficiency is } 52\% / W, \text{ defined as}$$

$$\eta_s = \frac{P_{SHG}^{out}}{(P_f^{in})^2} \times 100\%. \text{ We believe that, by optimizing device fabrication conditions,}$$

further enhancement of the wavelength conversion efficiency can be obtained.

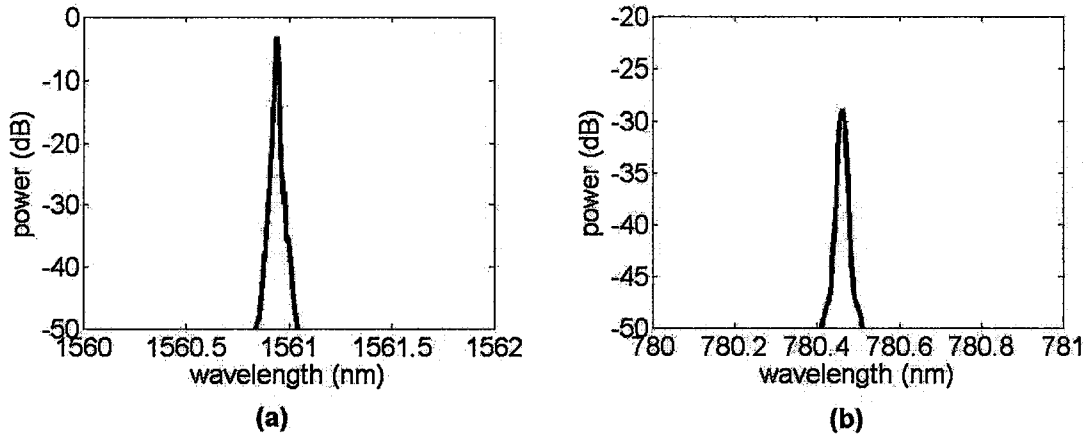


Fig. 5.3 spectrum of a) fundamental wave and b) second harmonic wave measured at output of the device

The SHG efficiency dependent on the fundamental power was measured and shown in Fig. 5.4 (dots with error bar), indicating good linearity over the tested power range. The average black box efficiency of the device is 41% /W,

which is defined as $\eta_b = \frac{P_{SHG}^{out}}{(P_f^{in})^2} \times 100\%$. The slop of the line in the Fig.5.4 is the

calculated curve, which shows good agreement with the measured data. In the calculation, the values of propagation losses at the fundamental and second harmonic wavelength are 0.6dB/cm and 1.3dB/cm, respectively. The value of effective area is $53 \mu m^2$ and poling quality is set as 75%.

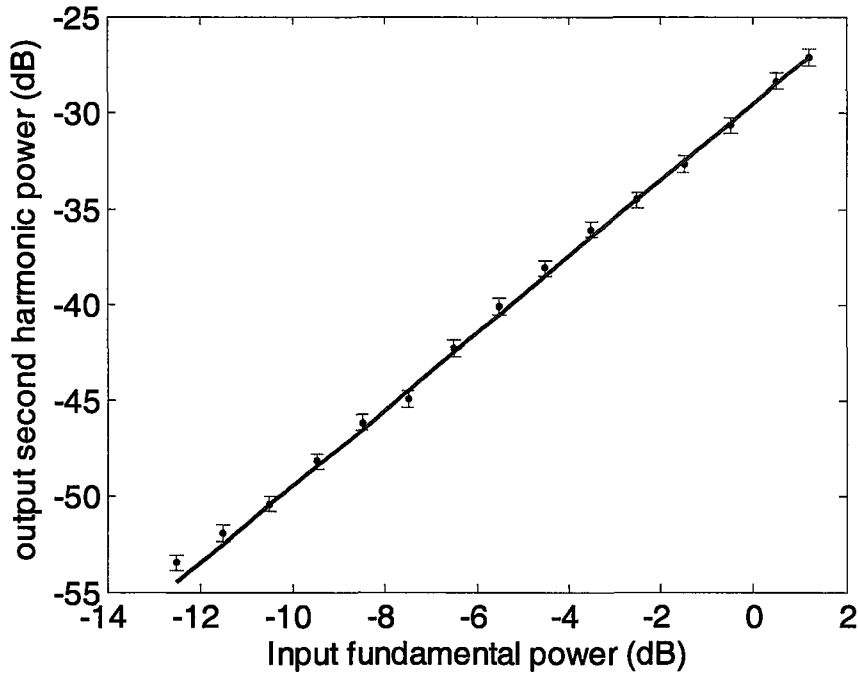


Fig.5.4 SHG power as functions of input pump power. The data fit well with the calculation.

The output wavelength of wavelength conversion device is tunable when device operating temperature is tuned. The QPM wavelength depending on temperature of PPMgO:LN is plotted in the Fig.5.5. The dots and the solid line represent the experimental and theoretical results, respectively. Measurements were performed between 25 °C and 120 °C . The device is held in a PPLN oven (from Thorlabs Inc.) with the oven house for 40mm long crystal, and its temperature was controlled by heater temperature controller TC200 with an accuracy of 0.1 °C . The linear curve indicates that the temperature sensitivity of the QPM wavelength shift is around 0.136 nm/°C for the device.

The temperature-tuning curve was calculated based on the temperature dependent Sellmeier equation for the extraordinary refractive index n_e (see 3.4). The QPM wavelength is determined by

$$\lambda_{QPM}(T) = 2\Lambda\Delta n_e(T) \quad (5.1)$$

where Λ is QPM period, Δn_e is the difference of extraordinary refractive index between the SHG light and the fundamental light.

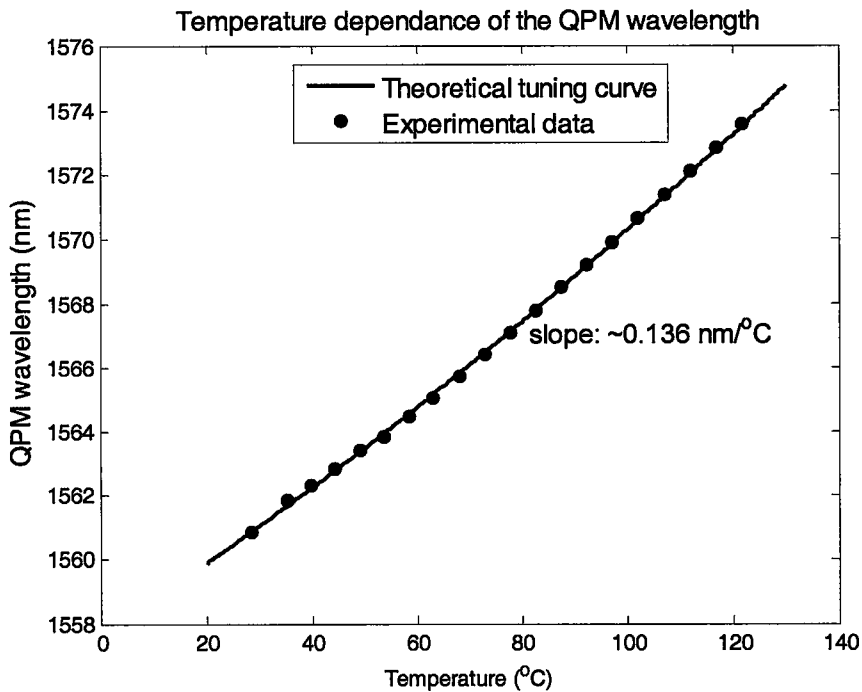


Fig.5.5 Temperature tuning curve for PPMgO:LN with QPM period $\Lambda = 19.5\mu\text{m}$

From the temperature dependent QPM wavelength, it is expected that the converted wavelength of DFG process can be tuned by changing device operation temperature and meanwhile the pump wavelength, indicating the possibility of variable-in variable-out wavelength conversions required in WDM network [21, 32].

5.4 External cavity Laser diode with fiber Bragg grating

In order to fully explore the performance of the DFG wavelength converter device, CW pump with stabilized wavelength around 780nm and power as large as tens of mW is necessary. Sources of this kind were not available in our lab at the time this experiment was planned, so one was designed and built specifically for this purpose. A typical configuration of external cavity Laser diode with fiber Bragg grating (FBG) is shown in Fig. 5.6 as block diagram and Fig. 5.7 as experimental setup. The optical cavity is defined by the Laser diode chip and the external FBG.

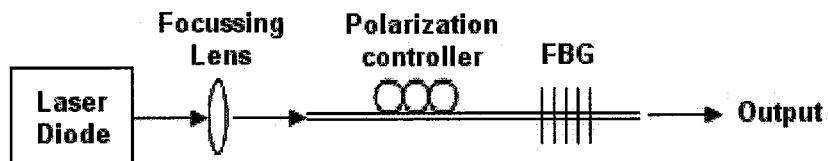


Fig.5.6 Block diagram of external cavity Laser diode with FBG

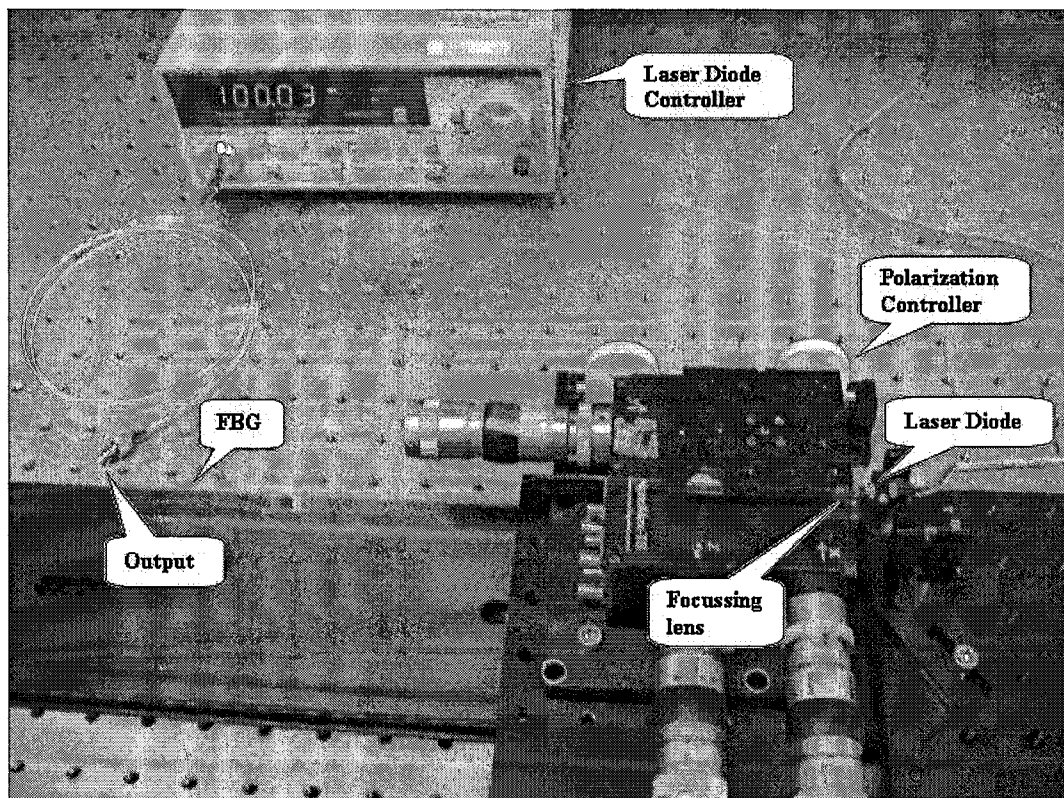


Fig.5.7 Experimental setup of the external cavity Laser diode with FBG

The FBG, positioned at a distance of 1–2 m from the Laser diode, acts as a wavelength-selective reflection filter. The FBG locks the Laser wavelength by the feedback of a small fraction of the Laser output at the Bragg wavelength. The reflection spectrum of the FBG filter is given by Fig.5.8. Peak wavelength λ_B , peak reflectivity R_{\max} , full-width at half-maximum (FWHM) reflection bandwidth of the FBG were measured to be 782.9nm, 18.5%, and 0.24nm, respectively.

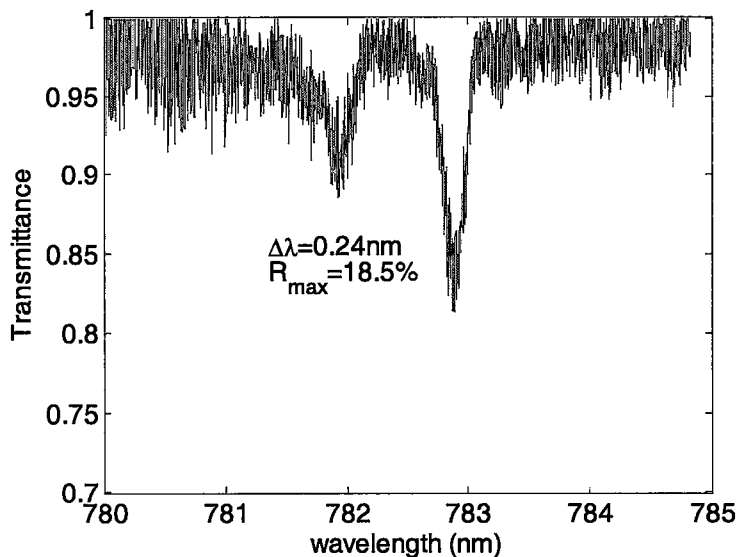


Fig.5.8 The measured transmission spectrum of the FBG.

The FBG provides tighter wavelength stability, but the additional feedback, together with the lens-fiber coupling, reduces the overall efficiency of the Laser, causing reduction in power from the order of 60 mW at the output of Laser diode to around 16 mW at the output of FBG. Fig.5.9 shows two emission spectra of the Laser diode with and without FBG stabilization, respectively. FBG effectively suppressed low-frequency (less than megahertz) power fluctuations and wavelength shifts with temperature and current, and locked emission light with an emission peak at the FBG wavelength of 783.0nm, as shown in Fig. 5.9 (a). The unlocked laser emits a broader spectrum peaking near the gain maximum at the wavelength of the free running laser as shown in Fig.5.9 (b).

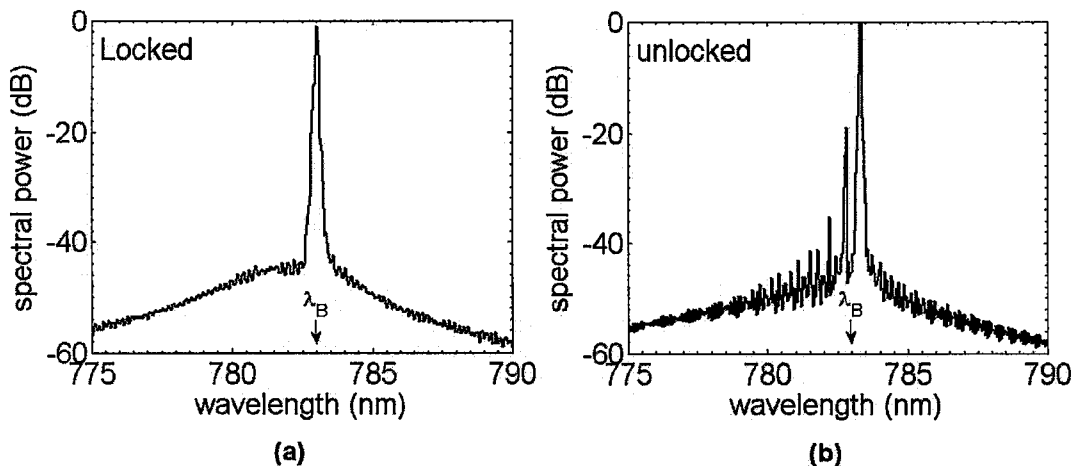


Fig.5.9 Typical emission spectrum of the Fabry-Perot Laser diode a) with FBG stabilization, b) without FBG stabilization

The fiber with the FBG at the end is a single-mode fiber (SMF) for wavelength of 780nm (numerical aperture: 0.14, mode field diameter at 750nm: $4.9 \mu\text{m}$). In the nonpolarization maintaining fiber, the initial linear state of polarization (SOP) of the emitted Laser light evolves to an arbitrary elliptical state upon propagation, due to random stresses within the fiber, bend-induced linear birefringence and twist-induced circular birefringence of the fiber core. The light reflected from the FBG into the laser cavity can undergo a change of polarization, thus the modification of the effective feedback strength has been shown to affect operating parameter of the Laser such as output power. Therefore, to maintain a pump Laser with power and wavelength stability over a wide range of operating condition, the proper fiber lay to minimize polarization change is of high concern. A polarization controller is used to manipulate the phase shift in the fiber and maintain the optimum fiber lay.

The FBG design provides effective feedback to keep the laser in the locked state. However, minor deviations from optimum fiber lay at operating condition introduce minor power and wavelength instability, which was the main difficulty in characterization of the DFG wavelength converter device.

5.5 Fiber Bragg grating

A fiber Bragg grating (FBG), shown in Fig.5.10, has periodical perturbation of the refractive index in the fiber core along the fiber length. It offers flexibility for Laser wavelength selection, and performs simple or more elaborated filtering functions. It is a key component for many applications in optical communications and sensing, such as routing, filtering, control and amplification of optical signals in wavelength division multiplexing (WDM) telecommunication networks, temperature, stress and pressure sensors, etc.

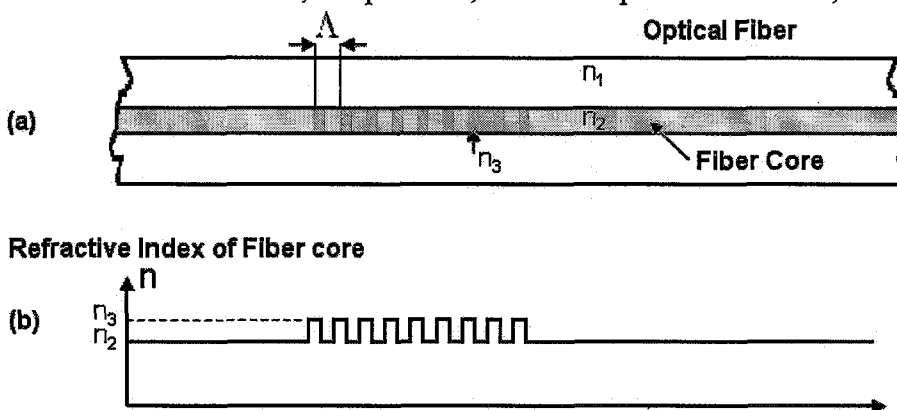


Fig.5.10 a) typical fiber Bragg grating structure and b) refractive index profile

The fundamental principle behind the operation of FBG is Fresnel reflection. Light travels through media of different refractive indexes will reflect and refract at the interface. The reflected wavelength λ_B , called the Bragg wavelength, is defined by the relationship,

$$\lambda_B = 2n_{eff}\Lambda \quad (5.2)$$

where n_{eff} is the average refractive index of the grating and Λ is the grating period.

Referring to Fig. 5.10, n_{eff} is the average of n_2 and n_3 . Any change in fiber properties, such as strain, temperature, or polarization which varies the refractive index or grating period will change the Bragg wavelength.

The fabrication of FBG is based on the photosensitivity of germanium doped optical fibers. When ultraviolet light radiates an optical fiber, the refractive index of the fiber is changed permanently; this effect is termed photosensitivity. The magnitude of the obtained refractive index change depends on several different factors such as the irradiation conditions (wavelength, intensity, and total dosage of irradiating light), the composition of glassy material forming the fiber core and any processing of the fiber prior to irradiation. The most commonly used UV light source is KrF excimer Laser that generate 248nm optical pulses (pulsewidth 10ns) at pulse repetition rates of 50~75 pulse/s. The wavelength of the UV source is selected to correspond to the absorption band of germanium-related glass defects. The typical irradiation conditions are an exposure to the laser light for a few minutes at intensities ranging for 100~1000 mJ/cm^2 . Prior to UV exposure, the fiber was loaded with hydrogen to enhance its photosensitivity. In the case of hydrogen loading, a refractive-index change of more than 1×10^{-2} can be obtained.[33]

One of the best fabrication techniques of FBGs is phase mask technique, which was originally introduced by Hill and Anderson, respectively, in 1993. [34, 35] The phase mask is made from flat slab of silica glass which is transparent to ultraviolet light. A one dimensional periodic surface relief structure is etched on one of the flat surfaces by photolithographic techniques. The shape of the periodic pattern approximates a square wave in profile. Fig.5.11 illustrates a typical scheme of phase mask grating fabrication method. The optical fiber is placed almost in contact with the corrugations of the phase mask. Ultraviolet light is incident normal to the phase mask and is diffracted by the periodic corrugations of the phase mask. Normally, most of the diffracted light is contained in the 0, +1 and -1 diffracted orders. However, the phase mask is designed to suppress the diffraction into the zero order by controlling the depth of the corrugations in the phase mask. In practice the amount of light in the zero-order can be reduced to less than 5% with approximately 40% of the total light intensity divided equally in the ± 1 orders. A periodic pattern to the core of optical fiber is produced by the two ± 1 diffracted order beams interfere pattern and the transmitted intensity of light striking the fiber. The period of the index grating is half of the period of the phase mask grating. Note that this period is independent of the wavelength of ultraviolet light irradiating the phase mask; however, the corrugation depth required to obtain reduced zero-order light is a function of the wavelength and the optical dispersion of the silica.[33] Phase mask used in our fabrication is chirped

fiber Bragg gratings, the grating period of which is varying along the length of the gratings.

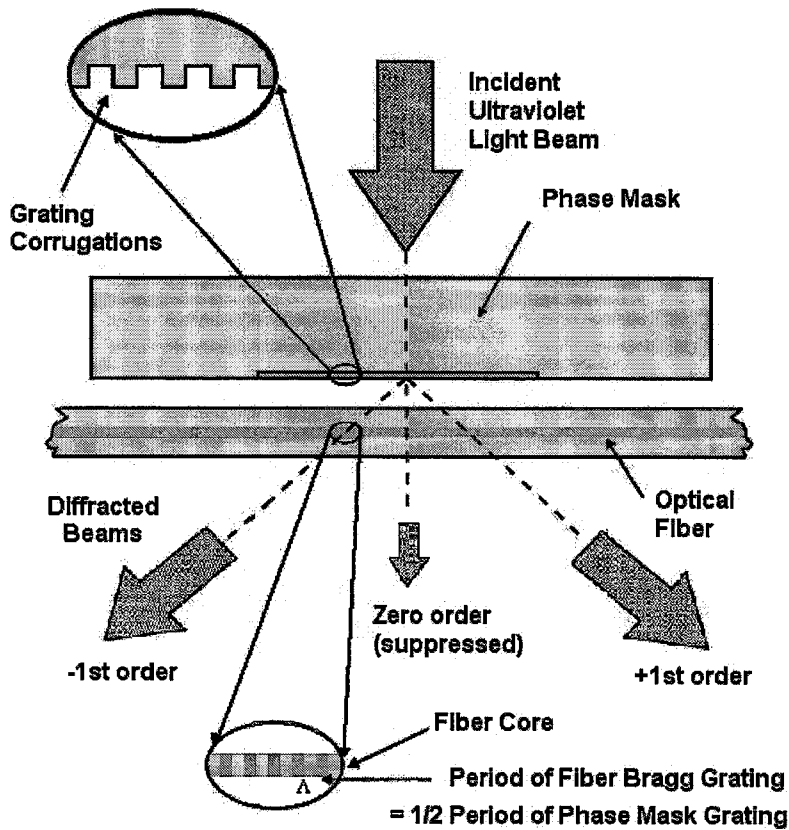


Fig.5.11 phase mask grating fabrication.[33]

5.6 DFG measurement

As described in Chapter 4, integrated coupling structure is a solution for the mode-launching issue in DFG wavelength conversion. In this section, DFG wavelength conversion was carried out to show the performance of the DFG wavelength converter with integrated coupling structure based on MgO doped lithium niobate.

DFG wavelength conversion generates an output at wavelength λ_{out} by mixing a strong pump laser light at wavelength λ_p with a weak signal laser light at wavelength λ_s , according to the parametric equation:

$$\frac{1}{\lambda_{out}} = \frac{1}{\lambda_p} - \frac{1}{\lambda_s} \quad (5.3)$$

DFG process allows conversion of multiple input wavelengths (or channels) as long as each individual channel is within the conversion bandwidth, where the phase matching condition is fulfilled and each set of input and output wavelengths follows the same parametric equation above.

The schematic diagram and experimental setup for DFG wavelength conversion measurement is shown in Fig.5.12. The external cavity Laser diode with fiber Bragg grating described in 5.4 was used as pump, at wavelength $\sim 783\text{nm}$. $1.5\text{-}\mu\text{m}$ band signal is from tunable Laser with the lasing wavelength tuned from 1510nm to 1640nm , and amplified by EDFA. These two beams were launched into two different waveguides via a fiber array, and combined into the wavelength converter by an integrated directional coupler. Annealed proton exchanged lithium niobate waveguides are polarization sensitive and guide only TM polarized light. The pump and signal light entering these waveguides must be properly polarized to maximize conversion efficiency. I used polarization controller to carefully adjust the polarization status of input light to be TM polarization, and polarization maintaining (PM) fiber to reduce polarization sensitivity. In PM fiber, the CW wave propagates in only one polarization direction. Output powers and spectra were measured by power meter and optical spectrum analyzer, respectively. The measurement can be taken at room temperature as MgO doped Lithium niobate significantly reduce the photorefractive effects, as mentioned in 3.1. However, the sample was maintained at 73°C for the requirement of the phase matching condition. The parameters of integrated coupler structure used in the DFG measurement are as follows.

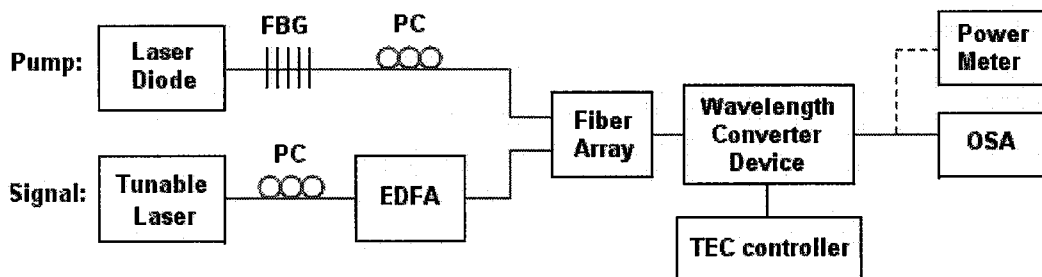


Fig.5.12 Schematic diagram for DFG wavelength conversion measurement. FBG: fiber Bragg grating. PC: polarization controller. OSA: optical spectrum analyzer.

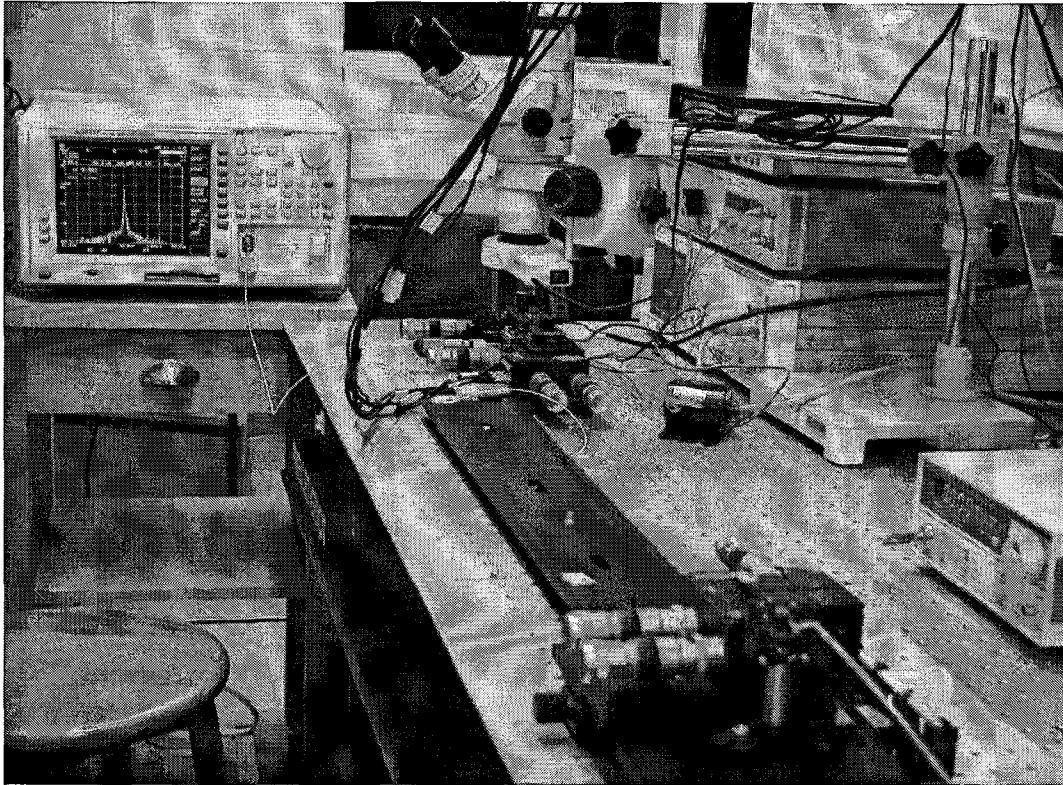


Fig.5.13 Experimental setup for DFG wavelength conversion measurement.

Conversion Efficiency

One of the most important requirements for practical application of a wavelength converter is high conversion efficiency. The conversion efficiency depends on several factors, such as pump power, device length, the passive insertion loss (including coupling loss and propagation loss), and the homogeneity of the structure.

$$\eta(\text{dB}) = 10 \log(P_{\text{out}} / P_s) \approx 10 \log(\eta_{\text{norm}} L^2 P_p) \text{ for } \eta_{\text{norm}} L^2 P_p < 1$$

The normalized efficiency η_{norm} for near degenerate DFG is similar to that of SHG theoretically. The power conversion efficiency is nearly proportional to the pump power in the limit of low conversion efficiency.

Fig. 5.14 shows a measured optical spectrum of wavelength conversion in log scale. The signal with wavelength of 1524.6nm is shifted by 85.8nm to an output wavelength of 1610.4nm. The QPM wavelength of the device is tuned at the pump wavelength by temperature tuning. The conversion efficiency of -29dB was obtained at the pump power of -1dB, which is much smaller than the value of -25dB estimated from the measured SHG efficiency. The discrepancy is probably because a part of the pump power propagated in modes other than the fundamental mode, as the pump input mode filter in the measurement is 4 μm wide and multimode waveguide for wavelength of 780 nm, instead of 2 μm wide and singlemode waveguide. Since conversion efficiency is proportional to the

pump power, an efficiency of -8 dB is expected if a pump power of $+20$ dBm is used.

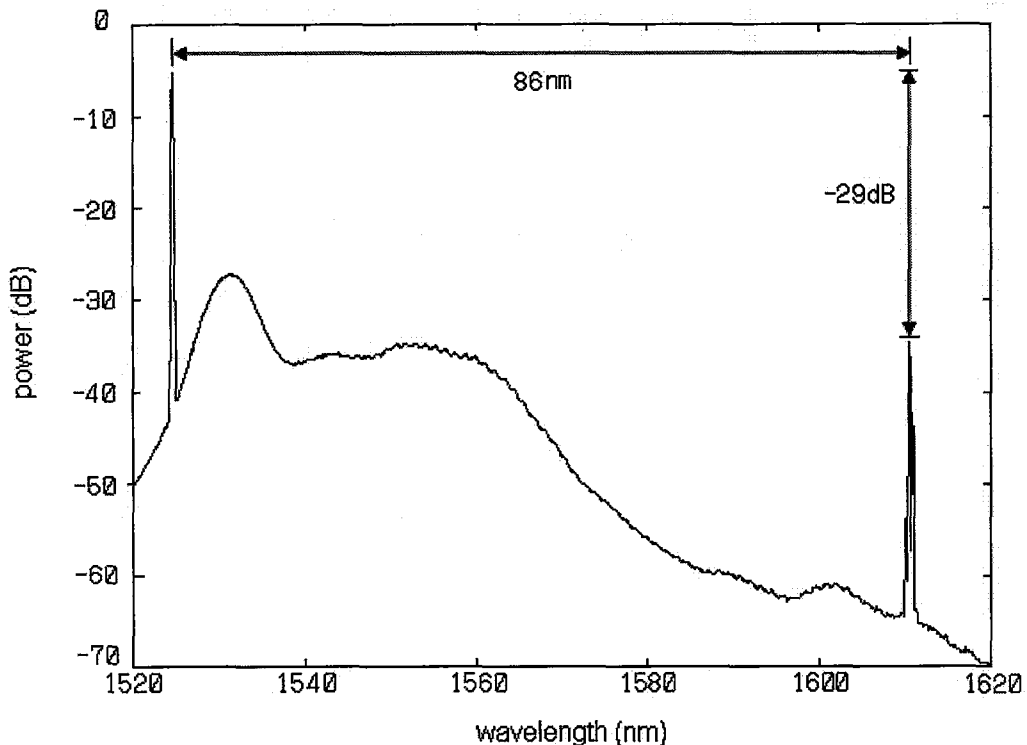


Fig. 5.14 Measured optical spectrum of a DFG experiment on a logarithmic scale of a signal at 1524.6nm and its converted output at 1610.4nm.

Conversion Bandwidth

The DFG wavelength converter has a wide conversion bandwidth due to the near-degenerate operation where the output wavelength moves in the opposite direction with respect to the signal wavelength tuning. The length and homogeneity, along with intrinsic material properties, also determine the bandwidth of the device. There are clearly tradeoffs between these factors. The conversion efficiency is proportional to the square of the interaction length, while the signal bandwidth is inversely proportional to the square root of the interaction length. Thus, longer devices have higher conversion efficiencies, but narrower bandwidths and stricter fabrication tolerances.

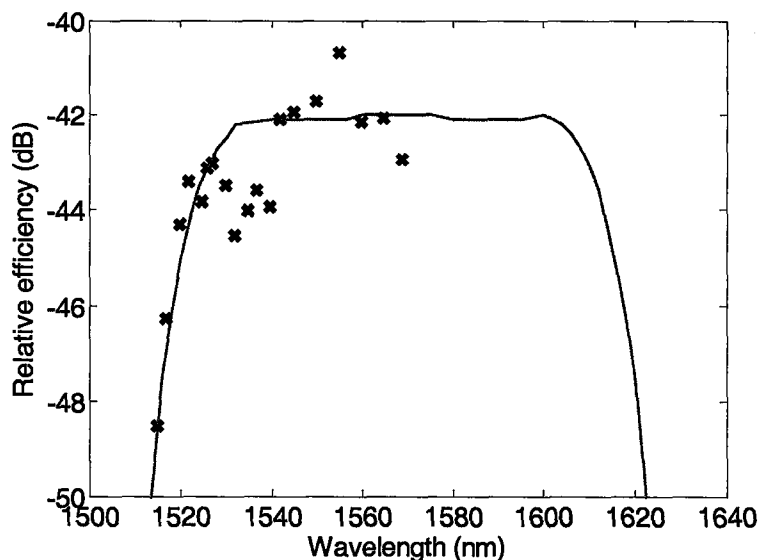


Fig.5.15 Relative conversion efficiency as a function of input signal wavelength. The cross marks are measured result, and the solid line is the theoretical prediction. The device has a 3-dB conversion bandwidth of 94 nm.

The pump wavelength is measured as 783nm, by tuning the input signal wavelength from 1510nm to 1570nm, the dependence of the wavelength conversion efficiency of the device on the signal wavelengths is shown in Fig.5.15. As seen in Eq. (2), the bandwidth of the device is determined by the condition whereby $\left(\Delta k - \frac{2\pi}{\Lambda}\right)L$ remains between $-\pi$ to $+\pi$. The device shows a 3-dB signal bandwidth of 94 nm. The device bandwidth can be broadened by detuning pump wavelength (tune operating temperature at the meantime) and/or using non-uniform QPM structures, which can be done as the next step of our research. The performance of DFG depends critically on the characteristics of the pump laser diode. The challenge of this experiment is the difficulty of maintaining a constant input pump at wavelength and in high power level for a long time. That is why the experimental results in Fig.5.15 fluctuate between a certain level, which value is much lower than the best result of conversion efficiency. For further measurement and research, a steady and high pump power is necessary.

Chapter 6

Conclusion

6.1 summary of research contributions

Lithium niobate wavelength converters are the preferred wavelength conversion devices in optical communications systems. The devices demonstrated in this work provide a solution in improving the conversion efficiency of wavelength converter for optical fiber communications.

This thesis has attempted to apply an integrated coupling structure on a MgO doped lithium niobate, in order to improve the conversion efficiency of the wavelength converter based on QPM periodic poled lithium niobate. MgO doped lithium niobate have greater photorefractive resistance compared to pure lithium niobate, allowing operation at high power and increase the conversion efficiency. The integrated coupling structure facilitates the coupling of the input waves into desired modes and optimizes the device coupling with the input fiber. This work offers a suitable design on components of integrated coupling structure, including mode filter, adiabatic tapers, directional couplers, and small-radius bends. A full theoretical analysis including waveguide modeling and simulation has been provided for each components of the structure. Consideration of losses, component length, efficiency and mode purity, affects the design of the device. Since the waveguide width is sensitive to the fabrication process, optimal design has been determined empirically. Several straight waveguides with different mask width has been fabricated to find the optimal mode filter. It has been found that 2 μm -wide mode filter for pump input is single mode waveguide and optimum for fiber pigtailling. It has a larger mode size than 8 μm -wide waveguide, indicating a nonlinear diffusion in fabrication process. Different taper profiles have also been examined. It is shown that an exponential profile has much less taper loss. A number of directional couplers with the same edge-to-edge separation of 2.5 μm has been fabricated with different waveguide widths (8~9 μm) and different interaction length (1.5~4 mm). It has shown that a directional coupler with length of 1.7mm and waveguide width of 8 μm is optimal, for its maximal coupling ratio of 25.4dB at $\lambda=1550$ nm.

The development of APE-PPMgO:LN fabrication techniques and integrated waveguide structures enables demonstrations of 1.5 μm band wavelength conversion based on DFG scheme for optical fiber communication. At first, the waveguide device has been characterized by SHG measurement and a nonlinear mixing efficiency of $\sim 450\%/W$ (\approx DFG efficiency) has been obtained. Then an external cavity Laser diode with FBG has been fabricated as a pump for the DFG demonstration. The performance and operation has been described. Finally, DFG process has been demonstrated in the telecommunication bands for the device with integrated coupling structure. The conversion efficiency of -29dB has been obtained at the pump power of -1dB. The experimental results have been

compared with the simulation, and discrepancies between the experimental results and the theoretical expectations have been explained. This structure represents the next generation of wavelength converter based on DFG process.

6.2 future researches

Despite the accomplishments of this research, a great deal remains to be done to increase the conversion efficiency of the wavelength converter. Improving waveguide design for nonlinear interaction is still necessary, better fabrication and waveguide modeling are required.

Device performance changes significantly by implementing several small changes in the waveguide design. Success relies on the good understanding of the waveguide based on the fabrication model and the observed device performance. The waveguide model that provides more accurate prediction of the concentration-dependent diffusion of protons in lithium niobate is needed for better device design. Controlling the waveguide fabrication process even better, we should be able to increase the uniformity of waveguide and periodic poled gratings, which would reduce the insertion loss of the device and increase the conversion efficiency.

References

- [1] C. Langrock, S. Kumar, J. E. McGeehan, A. E. Willner, and M. M. Fejer, "All-optical signal processing using $\chi^{(2)}$ nonlinearities in guided-wave devices," *Journal of Lightwave Technology*, vol. 24, pp. 2579-2592, Jul 2006.
- [2] E. B. F. Le Poux, E. Brandon, L. Buet, N. Darbois, V. Havard, L. and L. P. Labrunie, A. Tran, and J. P. Blondel, "25 GHz spaced DWDM 160*10.66 Gbit/s (1.6 Tbit/s) Unrepeated Transmission over 380 km," *Proceeding of ECOC'01*, pp. 21-23, 2001.
- [3] M.-H. Chou, "Optical Frequency Mixers Using Three-Wave Mixing for Optical Fiber Communications," in *Applied Physics*. vol. Doctor of Philosophy: Standard University, 1999.
- [4] S. J. B. Yoo, "Wavelength conversion technologies for WDM network applications," *Journal of Lightwave Technology*, vol. 14, pp. 955-966, Jun 1996.
- [5] a. H. T. Yasuhiro Suzuki, "Recent Research and Development of All-Optical Wavelength Conversion Devices," *NTT R D*, vol. 51, pp. 693-698, 2002.
- [6] M. Asobe, Y. Nishida, O. Tadanaga, H. Miyazawa, and H. Suzuki, "Wavelength conversion using quasi-phase matched LiNbO₃ waveguides," *Ieice Transactions on Electronics*, vol. E88C, pp. 335-341, Mar 2005.
- [7] M. H. Chou, J. Hauden, M. A. Arbore, and M. M. Fejer, "1.5- μ m-band wavelength conversion based on difference-frequency generation in LiNbO₃ waveguides with integrated coupling structures," *Optics Letters*, vol. 23, pp. 1004-1006, Jul 1998.
- [8] H. C. Guo, S. H. Tang, Z. D. Gao, Y. Q. Qin, S. N. Zhu, and Y. Y. Zhu, "Multiple-channel mid-infrared optical parametric oscillator in periodically poled MgO : LiNbO₃," *Journal of Applied Physics*, vol. 101, p. 5, Jun 2007.
- [9] R. W. Boyd, *Nonlinear optics*: Academic Press, 2003.
- [10] C. Q. Xu, H. Okayama, and M. Kawahara, "OPTICAL FREQUENCY CONVERSIONS IN NONLINEAR MEDIUM WITH PERIODICALLY MODULATED LINEAR AND NONLINEAR-OPTICAL PARAMETERS," *Ieee Journal of Quantum Electronics*, vol. 31, pp. 981-987, Jun 1995.
- [11] T. Suhara and M. Fujimura, *waveguide Nonlinear-Optic Devices*: Springer-Verlag Berlin Heidelberg, 2003.
- [12] M. M. Fejer, G. A. Magel, D. H. Jundt, and R. L. Byer, "QUASI-PHASE-MATCHED 2ND HARMONIC-GENERATION - TUNING AND TOLERANCES," *Ieee Journal of Quantum Electronics*, vol. 28, pp. 2631-2654, Nov 1992.

- [13] K. R. Parameswaran, "Highly Efficient Optical Frequency Mixers," in *Electrical Engineering*. vol. Doctor of Philosophy: Stanford University, 2002.
- [14] M. H. Hiroshi Nishihara, Toshiaki Suhara, *Optical Integrated Circuits*: McGraw-Hill Book Company, 1989.
- [15] K. Gallo, M. De Micheli, and P. Baldi, "Parametric fluorescence in periodically poled LiNbO₃ buried waveguides," *Applied Physics Letters*, vol. 80, pp. 4492-4494, Jun 2002.
- [16] I. Shoji, T. Kondo, A. Kitamoto, M. Shirane, and R. Ito, "Absolute scale of second-order nonlinear-optical coefficients," *Journal of the Optical Society of America B-Optical Physics*, vol. 14, pp. 2268-2294, Sep 1997.
- [17] Y. Nishida, H. Miyazawa, M. Asohe, O. Tadanaga, and H. Suzuki, "Direct-bonded QPM-LN ridge waveguide with high damage resistance at room temperature," *Electronics Letters*, vol. 39, pp. 609-611, Apr 2003.
- [18] R. M. Kumar, F. Yamamoto, J. Ichikawa, H. Ryoken, I. Sakaguchi, X. Liu, M. Nakamura, K. Terabe, S. Takekawa, H. Haneda, and K. Kitamura, "SIMS-depth profile and microstructure studies of Ti-diffused Mg-doped near-stoichiometric lithium niobate waveguide," *Journal of Crystal Growth*, vol. 287, pp. 472-477, Jan 2006.
- [19] N. Goto and G. L. Yip, "CHARACTERIZATION OF PROTON-EXCHANGE AND ANNEALED LINBO₃ WAVE-GUIDES WITH PYROPHOSPHORIC ACID," *Applied Optics*, vol. 28, pp. 60-65, Jan 1989.
- [20] Y. N. Korkishko and V. A. Fedorov, "Structural and optical characterization of annealed proton exchanged LiNbO₃ optical waveguides," *Optical Materials*, vol. 5, pp. 175-185, Mar 1996.
- [21] M. L. Bortz and M. M. Fejer, "ANNEALED PROTON-EXCHANGED LINBO₃ WAVE-GUIDES," *Optics Letters*, vol. 16, pp. 1844-1846, Dec 1991.
- [22] Y. N. Korkishko, V. A. Fedorov, T. M. Morozova, F. Caccavale, F. Gonella, and F. Segato, "Reverse proton exchange for buried waveguides in LiNbO₃," *Journal of the Optical Society of America a-Optics Image Science and Vision*, vol. 15, pp. 1838-1842, Jul 1998.
- [23] J. M. Zavada, H. C. Casey, R. J. States, S. W. Novak, and A. Loni, "CORRELATION OF SUBSTITUTIONAL HYDROGEN TO REFRACTIVE-INDEX PROFILES IN ANNEALED PROTON-EXCHANGED Z-CUT AND X-CUT LINBO₃," *Journal of Applied Physics*, vol. 77, pp. 2697-2708, 1995.
- [24] Y. N. Korkishko, V. A. Fedorov, S. M. Kostritskii, E. I. Maslennikov, M. V. Frolova, A. N. Alkaev, C. Sada, N. Argiolas, and M. Bazzan, "Proton-exchanged waveguides in MgO-doped LiNbO₃: Optical and structural properties," *Journal of Applied Physics*, vol. 94, pp. 1163-1170, Jul 2003.
- [25] X. F. Cao, R. V. Ramaswamy, and R. Srivastava, "CHARACTERIZATION OF ANNEALED PROTON EXCHANGED

- LINBO3 WAVE-GUIDES FOR NONLINEAR FREQUENCY-CONVERSION," *Journal of Lightwave Technology*, vol. 10, pp. 1302-1313, Sep 1992.
- [26] M. L. Bortz, "Quasi-phases-matched Optical Frequency Conversion in Lithium Niobate Waveguides," in *Applied Physics*. vol. Ph.D.: Stanford University, 1994.
- [27] A. Loni, R. W. Keys, and R. M. Delarue, "CHARACTERIZATION OF WAVE-GUIDES FORMED BY PROTON-EXCHANGE IN MGO-DOPED AND ND-MGO-DOPED LINBO3 - A COMPARISON WITH CONGRUENT MATERIAL," *Journal of Applied Physics*, vol. 67, pp. 3964-3967, May 1990.
- [28] M. M. Howerton, W. K. Burns, P. R. Skeath, and A. S. Greenblatt, "DEPENDENCE OF REFRACTIVE-INDEX ON HYDROGEN CONCENTRATION IN PROTON EXCHANGED LINBO3," *Ieee Journal of Quantum Electronics*, vol. 27, pp. 593-601, 1991.
- [29] H. P. Li, D. Y. Tang, S. P. Ng, and J. Kong, "Temperature-tunable nanosecond optical parametric oscillator based on periodically poled MgO : LiNbO3," *Optics and Laser Technology*, vol. 38, pp. 192-195, Apr 2006.
- [30] D. H. Jundt, "Temperature-dependent Sellmeier equation for the index of refraction, $n(e)$, in congruent lithium niobate," *Optics Letters*, vol. 22, pp. 1553-1555, Oct 1997.
- [31] D. A. Bryan, R. Gerson, and H. E. Tomaschke, "INCREASED OPTICAL-DAMAGE RESISTANCE IN LITHIUM-NIOBATE," *Applied Physics Letters*, vol. 44, pp. 847-849, 1984.
- [32] B. Chen, C. Q. Xu, B. Zhou, Y. Nihei, A. Harada, and Y. Wang, "Temperature characteristics of 1.5- μ m-band MgO doped LiNbO3 quasi-phase matched wavelength converters," *Japanese Journal of Applied Physics Part 2-Letters*, vol. 40, pp. L612-L614, Jun 2001.
- [33] K. O. Hill and G. Meltz, "Fiber Bragg grating technology fundamentals and overview," *Journal of Lightwave Technology*, vol. 15, pp. 1263-1276, Aug 1997.
- [34] K. O. Hill, B. Malo, F. Bilodeau, D. C. Johnson, and J. Albert, "BRAGG GRATINGS FABRICATED IN MONOMODE PHOTSENSITIVE OPTICAL FIBER BY UV EXPOSURE THROUGH A PHASE MASK," *Applied Physics Letters*, vol. 62, pp. 1035-1037, Mar 1993.
- [35] D. Z. Anderson, V. Mizrahi, T. Erdogan, and A. E. White, "PRODUCTION OF IN-FIBER GRATINGS USING A DIFFRACTIVE OPTICAL-ELEMENT," *Electronics Letters*, vol. 29, pp. 566-568, Mar 1993.

